

Excerpt from:
**Charge Density Wave Order in
Cuprate Superconductors Studied by
Resonant Soft X-ray Scattering**

by

Andrew Achkar

A thesis
presented to the University of Waterloo
in fulfillment of the
thesis requirement for the degree of
Doctor of Philosophy
in
Physics

Waterloo, Ontario, Canada, 2015

© Andrew Achkar 2015

Table of Contents

1 Resonant soft x-ray scattering	1
1.1 Overview	1
1.2 Basic theory of resonant elastic x-ray scattering	2
1.2.1 Diffraction	2
1.2.2 Quantum mechanical origin of resonant scattering	5
1.2.3 Atomic scattering form factor	10
1.2.3.1 Kramers-Kronig dispersion relations	12
1.2.4 The polarization dependence in REXS	16
1.3 Experimental methods	18
1.3.1 Beamline	18
1.3.2 Diffractometer and detectors	19
1.3.3 Sample preparation	24
APPENDICES	30
A Useful formulae and calculations	31
A.1 Relation between Miller indices and $(\theta, 2\theta)$ in a 2-circle scattering geometry	32
A.2 Wedge angle for azimuthal rotation experiment	34
A.3 Photon path lengths	35
References	36

Chapter 1

Resonant soft x-ray scattering

1.1 Overview

Resonant soft x-ray scattering (RSXS) is a technique that extends conventional x-ray diffraction (XRD) beyond the study of atomic positions in order to gain element, site, valence and orbital specific information about ordered states of matter. This specificity is gained by tuning the photon energy to an x-ray absorption edge, providing sufficient energy to excite an inner-shell core electron into an empty valence state and altering the anomalous components of the atomic scattering form factor such that it depends strongly on photon energy, photon polarization and the electronic environment of the scatterers. This resonant effect enhances the scattering amplitude, making it possible to detect weak ordering signatures, and embeds a wealth of information about the charge, spin and orbital degrees of freedom of the electronic order into the scattering process. In transition metal (TM) oxides, most of the interesting physics occurs at low energies, near the Fermi level of the transition metal ion. These low-lying empty states can be probed using soft x-rays ($\hbar\omega \sim 50\text{-}2000\text{ eV}$) which can resonantly excite the strong $2p \rightarrow 3d$, $3d \rightarrow 4f$, and $4d \rightarrow 5f$ dipole-allowed transitions of TM ions. In contrast, hard x-rays ($\hbar\omega > 10\text{ keV}$) are less useful for transition metal ions, since they probe the $4p$ states well above the Fermi energy via the $1s \rightarrow 4p$ transition.

Over the past two decades, the impact and importance of RSXS has grown significantly thanks to numerous advances in instrumentation and the theory of the resonant scattering.^[1] Third generation synchrotrons have provided simple control of the incident photon energy and polarization (thanks to elliptically polarizing undulators [2]), while providing very high photon flux, excellent energy resolution (eg. a resolution of $\Delta E \sim 0.1$

eV at $E = 1000$ eV is typical at most soft x-ray beamlines), better electron orbit stability and improved x-ray beam focusing properties.[3] Notable advances in the theory of resonant scattering have included the discovery of polarization dependence to anomalous scattering,[4] the appearance of forbidden reflections due to anisotropic x-ray susceptibility in crystals,[5] the theoretical description of magnetic resonant x-ray diffraction,[6, 7] and the development of frameworks to calculate resonant inelastic x-ray scattering spectra.[8, 9]

In this chapter, fundamental aspects of elastic RSXS will be presented. A theoretical treatment tailored to supplement the following chapters is presented in [section 1.2](#). More exhaustive reviews of the theory of resonant scattering are available.[10, 11, 12, 13, 14, 15, 16, 17] Experimental details particular to the REIXS beamline at the Canadian Light Source will be discussed in [section 1.3](#).

1.2 Basic theory of resonant elastic x-ray scattering

1.2.1 Diffraction

The diffraction of x-rays by crystals, structures composed of periodic arrangements of atoms that form a Bravais lattice,[18] was discovered in 1912 and has had an immeasurable impact on a vast array of disciplines.[19, 20] When a plane wave of the form $e^{i\mathbf{k}\cdot\mathbf{r}}$ is incident on periodic lattice of atoms, each atom causes a scattered radial wave of the form $fe^{i\mathbf{Q}\cdot\mathbf{r}}/r$ (for non-zero scattering angle),[21] where f is the atomic scattering form factor of the scattering atom. In a classical picture, this coincides with the incident wave causing an electron to vibrate and behave like a dipole that emits a radial wave with a scattering amplitude of f . Far from the scatterer, the emitted radial wave can be approximated by a plane wave. Constructive interference of many of such emitted plane waves from atoms in a lattice occurs when the difference in path length for plane waves arising from crystal planes that are separated by a distance d is an integer multiple of the wavelength. This describes the famous Bragg formulation of diffraction,[22] governed by the equation $n\lambda = 2d_{HKL} \sin \theta$, where λ is the x-ray wavelength, d_{HKL} is the interplanar separation (for a given set of lattice planes with Miller indices H , K , and L), θ is the scattering angle and n is the order of the interference.

Alternatively, it is possible to sum the emitted plane waves keeping track of their relative phases and arrive at the Laue condition for diffraction, $\mathbf{k}' - \mathbf{k} = \mathbf{G}$, where \mathbf{G} is a vector of the reciprocal lattice.[23] The Laue formulation is more useful when dealing with diffraction from a single crystal composed of multiple atom types, and it is more explicitly

written as a set of three simultaneous equations.[23]

$$\begin{aligned}\mathbf{a}_1 \cdot (\mathbf{k}' - \mathbf{k}) &= 2\pi H \\ \mathbf{a}_2 \cdot (\mathbf{k}' - \mathbf{k}) &= 2\pi K \\ \mathbf{a}_3 \cdot (\mathbf{k}' - \mathbf{k}) &= 2\pi L\end{aligned}\tag{1.1}$$

Here, \mathbf{a}_1 , \mathbf{a}_2 and \mathbf{a}_3 are the primitive vectors of the crystal lattice and H , K and L are Miller indices for a reciprocal lattice vector \mathbf{G} that satisfies $\mathbf{G} = H\mathbf{b}_1 + K\mathbf{b}_2 + L\mathbf{b}_3$, where \mathbf{b}_1 , \mathbf{b}_2 and \mathbf{b}_3 are the basis vectors for the reciprocal lattice.[24]

To account for the rotation of the crystal, and simplifying the problem to consider only cubic, tetragonal or orthorhombic lattices, it is useful to write $\mathbf{a}_{(1,2,3)} = (a, b, c)R\mathbf{O}_{(a,b,c)}$, where a , b and c are lattice constants, $\mathbf{O}_{(a,b,c)}$ are the initial orientation vectors of the crystal axes in the diffractometer frame (eg. for a horizontal scattering geometry, \hat{x} =primary beam direction, \hat{z} =vertical direction, \hat{y} =perpendicular to \hat{x} and \hat{z} in horizontal plane) and R is a rotation matrix that rotates the crystal axes by the diffractometer's rotations (eg. $R = R_{\theta_s} \cdot R_\chi \cdot R_\phi$). If one eliminates ϕ and χ rotations and considers only horizontal plane scattering, then it is possible to show that for a crystal with initial orientation $\mathbf{O}_a = -\hat{x}$ and $\mathbf{O}_b = \hat{y}$, the sample rotation angle θ_s and the detector angle 2θ are related to $\mathbf{Q} = 2\pi(H/a, K/b)$ according to:

$$2\theta = 2\sin^{-1} \left(\frac{hc}{2E} \sqrt{\left(\frac{H}{a}\right)^2 + \left(\frac{K}{b}\right)^2} \right)\tag{1.2}$$

$$\theta_s = \theta - \tan^{-1} \left(\frac{H}{K} \frac{b}{a} \right),\tag{1.3}$$

where h is Planck's constant, c is the speed of light in vacuum and E is photon energy.¹ Equations 1.2 and 1.3 are very useful for RSXS, since soft x-ray diffractometers typically operate in a 2-circle mode (fixed χ and ϕ) with the detector kept in the scattering plane. However, use of Eq. 1.1 can in principle be used to calculate scattering geometries for H , K and L indices in 3- and 4- circle modes. In practice, many diffractometers are typically running the scientific diffraction software **spec**, that includes a program called **fourc**.[25] This program implements a general form of Eq. 1.1, based on previously established calculations,[26] that can automatically calculate appropriate scattering geometries for requested reciprocal lattice vectors, provided that the crystal parameters and initial crystal orientation are set correctly.

¹See Section A.1 for a derivation of these equations.

As mentioned previously, the Laue formulation consists of summing up the plane waves emitted by all the atoms in a crystal. This approach is useful as it provides a way to calculate the scattering intensity as a function of \mathbf{Q} , the incident and emitted photon polarization vectors $\boldsymbol{\epsilon}$ and $\boldsymbol{\epsilon}'$, and the photon energy $E = \hbar\omega$. Assuming (for now) that the quantum mechanical light-matter interaction that occurs when a plane wave interacts with an atom in a crystal can be fully captured by the atomic scattering form factor $f \rightarrow f(\omega, \boldsymbol{\epsilon}, \boldsymbol{\epsilon}')$, it is possible to write down an expression for the scattering intensity in terms of this sum.[15, 17]

$$I(\mathbf{Q}, \omega, \boldsymbol{\epsilon}, \boldsymbol{\epsilon}') \propto \left| \sum_j f_j(\omega, \boldsymbol{\epsilon}, \boldsymbol{\epsilon}') e^{i\mathbf{Q} \cdot \mathbf{R}_j} \right|^2 \quad (1.4)$$

In Eq. 1.4, the sum is over all atomic sites j , with atomic positions denoted by \mathbf{R}_j . Following others, it is illustrative to index the coordinate system differently. If \mathbf{R}_j is instead written as $\mathbf{C}_m + \mathbf{r}_j$, where \mathbf{C}_m points to the center of unit cell m and \mathbf{r}_j locates the atoms within the unit cell relative to \mathbf{C}_m , then the scattering intensity can be separated into two components: a unit cell structure factor $F(\omega, \boldsymbol{\epsilon}, \boldsymbol{\epsilon}')$ and a lattice component $L(\mathbf{Q})$.

$$\begin{aligned} I(\mathbf{Q}, \omega, \boldsymbol{\epsilon}, \boldsymbol{\epsilon}') &\propto \left| \sum_{m,j} f_j(\omega, \boldsymbol{\epsilon}, \boldsymbol{\epsilon}') e^{i\mathbf{Q} \cdot (\mathbf{C}_m + \mathbf{r}_j)} \right|^2 \\ &= \left| \sum_j f_j(\omega, \boldsymbol{\epsilon}, \boldsymbol{\epsilon}') e^{i\mathbf{Q} \cdot \mathbf{r}_j} \right|^2 \times \left| \sum_m e^{i\mathbf{Q} \cdot \mathbf{C}_m} \right|^2 \\ &= |F(\omega, \boldsymbol{\epsilon}, \boldsymbol{\epsilon}')|^2 \times |L(\mathbf{Q})|^2 \end{aligned} \quad (1.5)$$

The lattice component has to do with interference of scattering arising from different unit cells whereas the unit cell structure factor describes interference coming from within the unit cell. In the limit that the number of unit cells goes to infinity, all the cells will scatter coherently (in phase) and $L(\mathbf{Q}) \propto \sum_{\mathbf{G}} \delta(\mathbf{Q} - \mathbf{G})$,[17, 21] which is a convenient way to arrive at the Laue condition (scattering occurs when $\mathbf{Q} = \mathbf{G}$).² This procedure also shows that for long range order, one only needs to calculate the unit cell structure factor in order to calculate the scattering intensity function.

²This derivation is shown neatly in Ref. [21], section 3.2.4.

1.2.2 Quantum mechanical origin of resonant scattering

The quantum mechanical origin of resonant scattering traces back to the interaction between an electromagnetic field and a Dirac (spin- $1/2$) particle. The general approach for finding the scattering amplitude is to treat either the Schrödinger Hamiltonian, the Schrödinger-Pauli Hamiltonian or the Dirac Hamiltonian, up to second order in perturbation theory.[27, 28, 15] To capture the interaction of an electron with the electromagnetic field, the momentum operator \mathbf{p} is replaced with $\mathbf{p} - e\mathbf{A}/c$, where \mathbf{A} is the vector potential of a quantized, time-dependent radiation field.

The approach I follow (as in Refs. [27, 29, 15]) is to consider the low energy limit ($E_{\text{x-ray}} \ll mc^2 \simeq 511 \text{ keV}$) of the Dirac Hamiltonian given by:

$$\mathcal{H}_D = \beta mc^2 + eV(\mathbf{r}) + c\boldsymbol{\alpha} \cdot [\mathbf{p} - e\mathbf{A}(\mathbf{r}, t)], \quad (1.6)$$

where β and $\boldsymbol{\alpha}$ are 4×4 Hermitian matrices (see Ref. [30] Sec. 3-2 or Ref. [31] for their properties), \mathbf{s}_i is the electron spin, $V(\mathbf{r})$ is the vector potential, and m is the electron mass. This approach is appropriate for scattering at almost all x-ray absorption edges (especially for soft x-rays $E_{\text{x-ray}} < 2 \text{ keV}$). It also has the benefit of resolving all the dominant resonant and non-resonant magnetic and non-magnetic terms that contribute to the scattering cross-section. It has been shown that Eq. 1.6 leads to the following matter-radiation interaction Hamiltonian, $\mathcal{H}_{\text{int}} = \mathcal{H}_1 + \mathcal{H}_2 + \mathcal{H}_3 + \mathcal{H}_4$, when small relativistic corrections are dropped.[27, 29, 15] The sum is over electrons labeled by index i .

$$\mathcal{H}_1 = + \sum_i \frac{e^2}{2mc^2} [\mathbf{A}(\mathbf{r}_i, t)]^2 \quad (1.7)$$

$$\mathcal{H}_2 = - \sum_i \frac{e^2 \hbar}{2m^2 c^4} \mathbf{s}_i [\partial_t \mathbf{A}(\mathbf{r}_i, t) \times \mathbf{A}(\mathbf{r}_i, t)] \quad (1.8)$$

$$\mathcal{H}_3 = - \sum_i \frac{e}{mc} [\mathbf{A}(\mathbf{r}_i, t) \cdot \mathbf{p}_i] \quad (1.9)$$

$$\mathcal{H}_4 = - \sum_i \frac{e\hbar}{mc} \mathbf{s}_i \cdot [\nabla \times \mathbf{A}(\mathbf{r}_i, t)] \quad (1.10)$$

Restricting our discussion to elastic scattering, we now consider how scattering events can occur through \mathcal{H}_{int} . An elastic scattering process can be defined as the interaction of a photon (ϵ, \mathbf{k}) with the electron system in a state $|G\rangle$ that results in the emission of a photon (ϵ', \mathbf{k}') and leaves the system in the final state $|G\rangle$ (for an elastic process $|\mathbf{k}| = |\mathbf{k}'|$). This can occur most simply by an interaction that absorbs (annihilates) the photon (ϵ, \mathbf{k})

and then emits a new photon (ϵ', \mathbf{k}') without causing any electronic transitions. Elastic scattering can also occur in cases where the absorption causes the electron to transition out of state $|G\rangle$ into an intermediate state $|I\rangle$ which subsequently decays back to $|G\rangle$ by emitting a photon. The former process is called non-resonant scattering and the latter is called resonant scattering.

We can understand these cases explicitly by checking how the four terms in \mathcal{H}_{int} act upon $|G\rangle$. To do this, we introduce a general quantized vector potential as an expansion in plane waves (with the Coulomb gauge $\nabla \cdot \mathbf{A} = 0$), given by

$$\mathbf{A}(\mathbf{r}, t) = \sum_{\mathbf{k}, \mu} \sqrt{\frac{hc}{V|\mathbf{k}|}} \left(a_{\mathbf{k}, \mu} \boldsymbol{\epsilon}_\mu(\mathbf{k}) e^{i(\mathbf{k} \cdot \mathbf{r} - \omega_{\mathbf{k}} t)} + a_{\mathbf{k}, \mu}^\dagger \boldsymbol{\epsilon}_\mu(\mathbf{k}) e^{-i(\mathbf{k} \cdot \mathbf{r} - \omega_{\mathbf{k}} t)} \right), \quad (1.11)$$

where V is the volume of the quantization box and $a_{\mathbf{k}}^\dagger$ and $a_{\mathbf{k}}$ are, respectively, photon creation and annihilation operators that operate on photons with wavevector \mathbf{k} and mode μ .³ The mode is conventionally represented by unit vectors that are either parallel to the scattering plane (π -polarization) or perpendicular to the scattering plane (σ -polarization) and in both cases perpendicular to the incident/scattered wave propagation directions.

The significance of Eq. 1.11 is that the vector potential is linear in the creation and annihilation operators, which means that it must operate twice on $|G\rangle$ in order for elastic scattering to occur.³ Hence, the terms \mathcal{H}_1 and \mathcal{H}_2 , which are both quadratic in \mathbf{A} , will contribute in first order to elastic scattering. To calculate the transition rate and ultimately the scattering cross-section, we first need calculate the matrix elements $M_1 = \langle G | \mathcal{H}_1 | G \rangle$ and $M_2 = \langle G | \mathcal{H}_2 | G \rangle$.^[32, 33, 29, 15, 17]

To obtain the dominant scattering contributions of \mathcal{H}_3 and \mathcal{H}_4 , which are both linear in \mathbf{A} , second order perturbation theory is needed. Following others,^[29, 15] the expression for the matrix elements $M_3 + M_4$ is given by

$$M_3 + M_4 = \sum_n \frac{\langle G | \mathcal{H}_3^* + \mathcal{H}_4^* | I_n \rangle \langle I_n | \mathcal{H}_3 + \mathcal{H}_4 | G \rangle}{\hbar \omega_{\mathbf{k}} - (E_n - E_g) + i\frac{\Gamma}{2}}, \quad (1.12)$$

where the system transitions from a ground state $|G\rangle$ with energy E_g into all n accessible intermediate states $|I_n\rangle$ with energy E_n and lifetime $\simeq \hbar/\Gamma$. The number of transitions

³To see why, simply consider that $(a + a^\dagger)$ acting on the vacuum state $|0\rangle$ gives $|0\rangle + |1\rangle$ and therefore does not preserve the number of photons. In contrast, $(a + a^\dagger)^2$ has four terms and when acting on $|0\rangle$ one of these terms that will first annihilate and then create a photon, as needed for scattering. It also has a term that will first create and then annihilate a photon and two terms that create/annihilate ± 2 photons, but these extra terms do not correspond to scattering.

per unit time w is then given by Fermi's golden rule and can be evaluated as

$$\begin{aligned} w &= \frac{2\pi}{\hbar} |M_1 + M_2 + M_3 + M_4|^2 \delta(\hbar\omega_{\mathbf{k}} - \hbar\omega_{\mathbf{k}'}) \\ &= \frac{2\pi}{\hbar} \left| \langle G | \mathcal{H}_1 + \mathcal{H}_2 | G \rangle + \sum_n \frac{\langle G | \mathcal{H}_3^* + \mathcal{H}_4^* | I_n \rangle \langle I_n | \mathcal{H}_3 + \mathcal{H}_4 | G \rangle}{\hbar\omega_{\mathbf{k}} - (E_n - E_g) + i\frac{\Gamma}{2}} \right|^2 \delta(\hbar\omega_{\mathbf{k}} - \hbar\omega_{\mathbf{k}'}) . \end{aligned} \quad (1.13)$$

This general expression can be used to calculate all the dominant contributions of charge and magnetic scattering for both resonant and non-resonant processes. While magnetic x-ray scattering is a deep and interesting subject, the studies contained within this thesis rely on charge scattering, so for simplicity I will now drop the terms M_2 and M_4 that contain the spin \mathbf{s} (see Refs. [34, 6, 7, 35, 29, 15] for more on magnetic x-ray scattering). Using Eq. 1.11, the matrix elements M_1 and M_3 become

$$\begin{aligned} M_1 &= \langle G | \sum_i \frac{e^2}{2m} [\mathbf{A}(\mathbf{r}_i, t)]^2 | G \rangle \\ &= \frac{hc}{V|\mathbf{k}|} \frac{e^2}{mc^2} (\boldsymbol{\epsilon}_{\mu'}^* \cdot \boldsymbol{\epsilon}_{\mu}) \sum_i \langle G | e^{i(\mathbf{k}-\mathbf{k}') \cdot \mathbf{r}_i} | G \rangle \end{aligned} \quad (1.14)$$

$$\begin{aligned} M_3 &= \sum_n \frac{\langle G | \sum_i \frac{e}{mc} [\mathbf{A}^*(\mathbf{r}_i, t) \cdot \mathbf{p}_i^*] | I_n \rangle \langle I_n | \sum_i \frac{e}{mc} [\mathbf{A}(\mathbf{r}_i, t) \cdot \mathbf{p}_i] | G \rangle}{\hbar\omega_{\mathbf{k}} - (E_n - E_g) + i\frac{\Gamma}{2}} \\ &= \frac{hc}{V|\mathbf{k}|m} \frac{e^2}{mc^2} \sum_n \frac{\langle G | \sum_{j=1}^N \boldsymbol{\epsilon}_{\mu'}^{*\dagger} \cdot \mathbf{p}_j e^{-i\mathbf{k}' \cdot \mathbf{r}_j} | I_n \rangle \langle I_n | \sum_{j'=1}^N \boldsymbol{\epsilon}_{\mu} \cdot \mathbf{p}_{j'} e^{i\mathbf{k} \cdot \mathbf{r}_{j'}} | G \rangle}{\hbar\omega_{\mathbf{k}} - (E_n - E_g) + i\frac{\Gamma}{2}} \end{aligned} \quad (1.15)$$

as shown in Ref. [29].

Given these matrix elements, the differential cross-section (i.e., the probability that a photon is scattered into a given solid angle $d\Omega$) can be calculated using the relations

$$\frac{d^2\sigma}{dEd\Omega} = \frac{w\rho(E)}{c/V}, \text{ and } \rho(E) = \frac{V}{(2\pi)^3} \frac{E^2}{\hbar^3 c^3} \quad (1.16)$$

where $\rho(E)$ is the density of photon states (in the quantization box of volume V) with energy that satisfies $\hbar\omega_{\mathbf{k}} \leq \hbar\omega_{\mathbf{k}'} + dE$. [34, 29] Substitution of the matrix elements into Eq. 1.13 and integration over energy (whereby the delta function ensures that only the elastic

scattering is included) gives

$$\frac{d\sigma}{d\Omega} = r_0^2 \left| (\boldsymbol{\epsilon}_{\mu'}^* \cdot \boldsymbol{\epsilon}_\mu) \sum_i \langle G | e^{i(\mathbf{k}-\mathbf{k}') \cdot \mathbf{r}_i} | G \rangle + \sum_n \frac{\langle G | \sum_{j=1}^N \boldsymbol{\epsilon}_{\mu'}^{*\prime} \cdot \mathbf{p}_j e^{-i\mathbf{k}' \cdot \mathbf{r}_j} | I_n \rangle \langle I_n | \sum_{j'=1}^N \boldsymbol{\epsilon}_\mu \cdot \mathbf{p}_{j'} e^{i\mathbf{k} \cdot \mathbf{r}_{j'}} | G \rangle}{\hbar\omega_{\mathbf{k}} - (E_n - E_g) + i\frac{\Gamma}{2}} \right|^2 \quad (1.17)$$

where $r_0 = e^2/(mc^2)$ is the classical electron radius. Note that the quantization box volume V is not present in this observable and all the pre-factors except r_0 have canceled out. It is now apparent that the first term is simply Thomson scattering, which has the usual polarization factor $(\boldsymbol{\epsilon}_{\mu'}^* \cdot \boldsymbol{\epsilon}_\mu)^2$ and is proportional to the square of the Fourier transform $F(\mathbf{Q})$ of the electron density $\rho(\mathbf{r})$, defined by

$$F(\mathbf{Q}) = \sum_i \langle G | e^{i\mathbf{Q} \cdot \mathbf{r}_i} | G \rangle = \int d\mathbf{r} e^{i\mathbf{Q} \cdot \mathbf{r}} \rho(\mathbf{r}). \quad (1.18)$$

The second term is the resonant charge scattering differential cross-section. This term can be further simplified if one takes the electric dipole approximation whereby the exponential term in Eq. 1.17 is expanded as $e^{-i\mathbf{k} \cdot \mathbf{r}_j} \sim (1 + i\mathbf{k} \cdot \mathbf{r}_j - (\mathbf{k} \cdot \mathbf{r}_j)^2/2 + \dots)$, keeping as many terms as needed for describing a particular process. For the resonant processes discussed here, only the first term contributes significantly. Multipole analysis involves keeping additional terms and has been covered in Refs. [34, 7, 10, 11, 15].

Keeping just the first term in the dipole approximation, the resonant scattering cross-section can be further simplified by replacing the momentum operator according to $\mathbf{p} = \frac{m}{ih}[\mathbf{r}, H_{el}] = \frac{m}{ih}\mathbf{r}(E_n - E_g)$, where H_{el} is the electron Hamiltonian that gives the energies of the ground and intermediate states. Using this commutator identity and dropping all pre-factors, the differential cross-section for electric dipole resonant scattering can be written

$$\left(\frac{d\sigma}{d\Omega} \right)_{\text{res.}} \propto \left| \sum_n \frac{\langle G | \boldsymbol{\epsilon}_{\mu'}^{*\prime} \cdot (\sum_j \mathbf{r}_j) | I_n \rangle \langle I_n | \boldsymbol{\epsilon}_\mu \cdot (\sum_j \mathbf{r}_j) | G \rangle}{\hbar\omega_{\mathbf{k}} - (E_n - E_g) + i\frac{\Gamma}{2}} \right|^2. \quad (1.19)$$

To illustrate the use of Eq. 1.19, it can further be shown (see Refs. [7, 11, 29]), that in the special case of atoms treated as free ions with spherical symmetry that is only broken by their magnetic moment, the differential cross-section simplifies to

$$\left(\frac{d\sigma}{d\Omega} \right)_{\text{res.}} \propto \left| \sum_n [(\boldsymbol{\epsilon}_{\mu'}^* \cdot \boldsymbol{\epsilon}_\mu) F^{(0)} - i(\boldsymbol{\epsilon}_{\mu'}^* \times \boldsymbol{\epsilon}_\mu) \cdot \mathbf{z}_n F^{(1)} + (\boldsymbol{\epsilon}_{\mu'}^* \cdot \mathbf{z}_n)(\boldsymbol{\epsilon}_\mu \cdot \mathbf{z}_n) F^{(2)}] \right|^2, \quad (1.20)$$

where the functions $F^{(0,1,2)}$ (as defined in Ref. [11], not to be confused with $F(\mathbf{Q})$) are related to the radial wave functions of the atomic states (in terms of spherical harmonics) and \mathbf{z}_n is a unit vector in the direction of the magnetic moment of the n^{th} ion.⁴ It may be surprising that although we previously dropped the terms with an explicit spin term, there is a reappearance of magnetic scattering here in the second and third terms of Eq. 1.20. This comes from the Pauli exclusion principle. Since the resonant scattering cross-section depends on the availability of states into which the core electron can transition and since the electron's spin is conserved during the transition, the transition rate will depend on whether the core electron has the same spin or opposite spin as the unoccupied state.[29] These unexpected resonant magnetic scattering terms are important, as they can be used to explain x-ray magnetic dichroism effects in x-ray absorption spectroscopy,[36, 37] and also do contribute to resonant magnetic x-ray scattering effects.

The specific case of a free ion with spherical symmetry is, however, not general nor always appropriate. Many ions in real crystals can have their spherical symmetry broken due to their electronic environment (e.g., octahedral, tetragonal or orthorhombic coordination) in addition to perhaps having a local magnetic moment. Such anisotropy often translates to magneto-optical effects, which will influence how an atom scatters light of a given polarization. Instead of representing the interaction term by a scalar quantity (complex or otherwise) a Cartesian tensor can be used.[4, 5]

An elegant treatment of this problem for x-ray scattering was recently presented.[38] With the atomic scattering form factor denoted as a tensor \hat{f} rather than a scalar quantity, the differential cross-section, or measured scattering intensity, is given by

$$I \propto \frac{d\sigma}{d\Omega} \propto \left| \sum_j (\epsilon'_{\mu'}^* \cdot \hat{f}_j \cdot \epsilon_{\mu}) e^{i\mathbf{Q} \cdot \mathbf{r}_j} \right|^2, \quad (1.21)$$

where the scattering tensor \hat{f}_j at atomic site j can be written, in the lowest possible symmetry (i.e., triclinic) and dropping the site index, as

$$\hat{f}(\omega) = \begin{pmatrix} f_{xx}(\omega) & f_{yx}(\omega) & f_{zx}(\omega) \\ f_{xy}(\omega) & f_{yy}(\omega) & f_{zy}(\omega) \\ f_{xz}(\omega) & f_{yz}(\omega) & f_{zz}(\omega) \end{pmatrix}. \quad (1.22)$$

The components of \hat{f}_j depend on photon energy and are complex. For systems with either cubic, tetragonal or orthorhombic symmetry, charge scattering contributions will

⁴Had we carried out the calculation including the matrix element M_4 , we would have found an extra contribution to the charge scattering term proportional to $(\epsilon' \cdot \epsilon)$; however, it turns out this correction is less than 1% of the above term so it is safe to neglect.[15]

only appear on the diagonal of this tensor but magnetic scattering contributions can appear on and off-diagonal and will generally depend on the direction of the local magnetization and the crystal symmetry.^[38] These diagonal charge terms will play a crucial role in Chapter ??, where the crystal symmetry and absence of sensitivity to magnetic order give a tensor of the form

$$\hat{f}_{\text{charge}} = \begin{pmatrix} f_{xx} & 0 & 0 \\ 0 & f_{yy} & 0 \\ 0 & 0 & f_{zz} \end{pmatrix}. \quad (1.23)$$

The tensorial representation of the scattering form factor has gained significance as the RSXS technique becomes more accessible and is used to study materials with increasingly complex magnetic structures or anisotropic crystal structures. However, prior to this development (and in cases where a full tensor is not needed) the complex, yet non-tensorial, atomic scattering form factor was (and is) used to calculate scattering intensities. I will now relate the atomic scattering form factor to the differential cross-section, show how it relates to the scattering tensor and highlight a practical, yet powerful, method of modelling resonant scattering processes.

1.2.3 Atomic scattering form factor

The relation between the differential cross-section and the atomic scattering form factor (also called the scattering length or scattering amplitude) is defined as

$$\frac{d\sigma}{d\Omega} = |f|^2. \quad (1.24)$$

This comes simply from the definition that the scattered wave will have its amplitude reduced by a factor of f as compared to the incident wave. Comparing Eq. 1.24 to Eq. 1.17, we can see that f can be decomposed into 3 terms⁵

$$\begin{aligned} f &= f^T + f' + if'' \\ f(\omega, \epsilon, \epsilon') &= f^T(\epsilon, \epsilon') + f'(\omega, \epsilon, \epsilon') + if''(\omega, \epsilon, \epsilon'), \end{aligned} \quad (1.25)$$

where f^T is the usual non-resonant Thomson form factor and $f' + if''$ is the anomalous scattering form factor (also called the dispersion correction). The first line in Eq. 1.25 is a shorthand form whereas the second line shows which terms depend explicitly on polarization and/or energy. While f^T is simply proportional to the number of electrons, we see

⁵Actually a fourth term, f^M should appear in Eq. 1.25, corresponding to the non-resonant magnetic scattering that would have been included if the matrix element M_2 wasn't dropped.

that $f' + if''$ comes from the second order perturbation in \mathcal{H}_3 , producing a photon energy dependent, complex quantity with a damped pole (resonance) at $\hbar\omega = E_n - E_g$. In this way, the atomic scattering form factor is clearly divided into a non-resonant and resonant contribution, both of which derive from the quantum mechanical interaction of an electromagnetic plane wave with an electron, as detailed in the previous section. Comparing terms in Eq. 1.4 and Eq. 1.21, it is apparent that f and \hat{f} are related by

$$f(\omega, \epsilon, \epsilon') = (\epsilon'^*_\mu \cdot \hat{f} \cdot \epsilon_\mu), \quad (1.26)$$

clarifying the link between the traditional atomic scattering form factor and the more general tensor representation.

If we suppose that we are dealing with spherical symmetry ($\hat{f} = fI_3$, where I_3 is the identity matrix) and an isolated atom, then it is possible to calculate f' and f'' for all the elements. This problem has been studied extensively, and the most complete and currently the “best” tabulation of such theoretical calculations for elements $Z = 1 - 92$ in the energy range $E = 1 - 10$ eV to $0.4 - 1$ MeV is given by combining the tables in Refs. [39, 40]. It is possible to obtain this data using the online resource at Ref. [41]. An empirical tabulation of the atomic scattering form factor is given in Ref. [42], which can also be accessed online.[43] For offline access, I have created a Mathematica notebook that loads these databases and can then provide f' and f'' for all the elements and arbitrary photon energy (this is posted publicly online, see Ref. [44]).

While the empirical and theoretical tabulations are largely convergent, there can be sizeable differences, particularly at very low photon energy $E < 100$ eV and in the near-edge regions. For an example of such differences, and to establish a general idea for how f depends on photon energy, Fig. 1.1 shows f' and f'' for Cu and O in the soft x-ray regime. The imaginary component (f'') has notable “step-like” features and the real part (f') has “poles” that coincide with these steps.

The so-called edge-steps come from an instantaneous jump in the $|G\rangle \rightarrow |I\rangle$ transition probability of the free-atom. If one has familiarity with x-ray absorption spectroscopy, it becomes apparent that f'' is related to the x-ray absorption cross-section. In fact, this comes from the terms in \mathcal{H}_3 that annihilate the incident photon but do not create a scattered photon,[17] and we can then identify that the differential cross-section for x-ray absorption is

$$\frac{d\sigma_{\text{abs}}}{d\Omega} = \frac{4\pi}{k} f''. \quad (1.27)$$

This relation defines the optical theorem,[45, 28] an important consequence of which is that the real and imaginary parts of the scattering amplitude satisfy the famous Kramers-Kronig dispersion relations.[46]

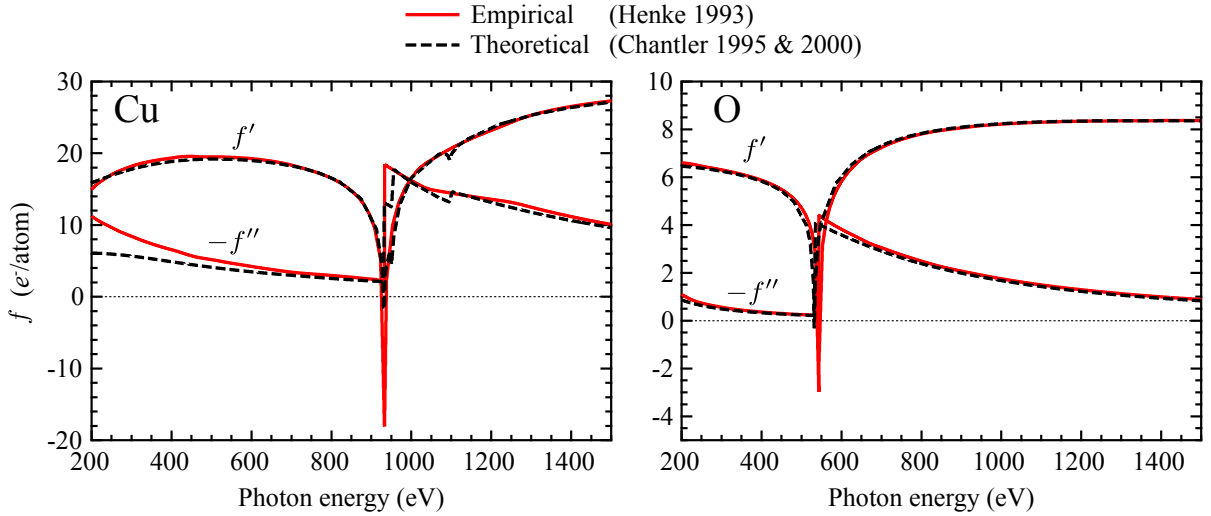


Figure 1.1 – The real and imaginary parts of the atomic scattering form factor for Cu (left) and O (right) tabulated for photon energies in the soft x-ray regime. The discontinuous jumps in f'' correspond to x-ray absorption edges. A finite-width pole (resonance) in f' occurs at the edges. Two sources are compared. The empirical data is interpolated from the available data in Ref. [42]. The theoretical data is from Ref. [39]

1.2.3.1 Kramers-Kronig dispersion relations

The Kramers-Kronig dispersion relations are

$$f'(E) = \frac{2}{\pi} \mathcal{P} \int_0^\infty \frac{E' f''(E)}{E'^2 - E^2} dE' \quad (1.28)$$

$$f''(E) = -\frac{2E}{\pi} \mathcal{P} \int_0^\infty \frac{f'(E)}{E'^2 - E^2} dE' \quad (1.29)$$

where the integral $\mathcal{P}\int$ denotes a Cauchy principal value integral. These are causal relations, strictly referring to the fact that a scattering event must first be preceded by an incident wave interacting with the scatterer.[46] The power of these relations is that it is generally possible to measure the x-ray absorption cross-section (eg., with an x-ray transmission experiment), and thus to empirically determine f'' as a function of energy. Given this, one can use Eq. 1.28 to determine $f'(E)$ and thus determine both f' and f'' from an x-ray absorption measurement. This is what was done in Ref. [42] to tabulate f' . Even in the case that a scattering tensor \hat{f} is needed, it is possible to measure the x-ray absorption with

the polarization vector aligned with the different crystal axes and build up the scattering tensor from these components (see Ref. [47] for an example of this done for YBCO).

As a slightly technical point, there are various integration schemes that can be found in the literature to deal with the principal value integral (see Refs. [42, 39] for two examples). These techniques are designed to succeed over a wide energy range by performing different integrations depending on whether the energy is near or far from an absorption edge. They are also coded in low level languages to ensure high speed. For the Kramers-Kronig transforms presented in Chapters ?? and ??, it was not crucial to reproduce these features, so I opted to implement the numerical integration in Mathematica. The key feature is that the numerical integral can simply be performed with a single (high level) function call of the form:

$$f'[E] := Z + \frac{2}{\pi} \text{NIntegrate} \left[\frac{E' f''[E']}{E'^2 - E^2}, \{E', 0, E, \infty\}, \text{Method} \rightarrow \left\{ \text{"PrincipalValue"}, \text{Method} \rightarrow \left\{ \text{"AdaptiveMonteCarlo"}, \text{"BisectionDithering"} \rightarrow 1/8 \right\}, \text{MaxRecursion} \rightarrow 200 \right], \right]$$

providing numerous options to control how NIntegrate is evaluated. Note that I have included the atomic number Z in this calculation to match the NIST definition for the real part of f , which includes the low- \mathbf{Q} limit of f^T (given simply by Z)⁶. To test this method, I calculated f' from the tabulated values of f'' for a variety of elements and compared them to the tabulated f' values. A few such calculations for O, Cu, C, K, Ba, and Pb are presented in Fig. 1.2. I have made the precise implementation used to generate these calculations publicly available at Ref. [48]. As can be seen, this method provides a very good approximation of the tabulated f' values over the full energy range.

The residuals do highlight that this integration method has difficulty converging at the absorption edges (where f'' is discontinuous). However, in a realistic use-case that I am considering, the tabulated near-edge values of f'' would be replaced by high resolution x-ray absorption data, such that the edge-jumps would either be smooth or small compared to the x-ray absorption near-edge structure. Consequently, this numerical integration method is generally quite reliable for the use case it targets. It is also worth pointing out the same integration strategy was used for all cases in Fig. 1.2, but it is very likely that better results can be achieved on a case-by-case basis by optimizing the strategy.

⁶This is approximate, as for very high energy a relativistic correction is needed, and Z should be replaced by $Z^* \approx Z - (Z/82.5)^2$,³⁷ relevant for high Z elements.[42]

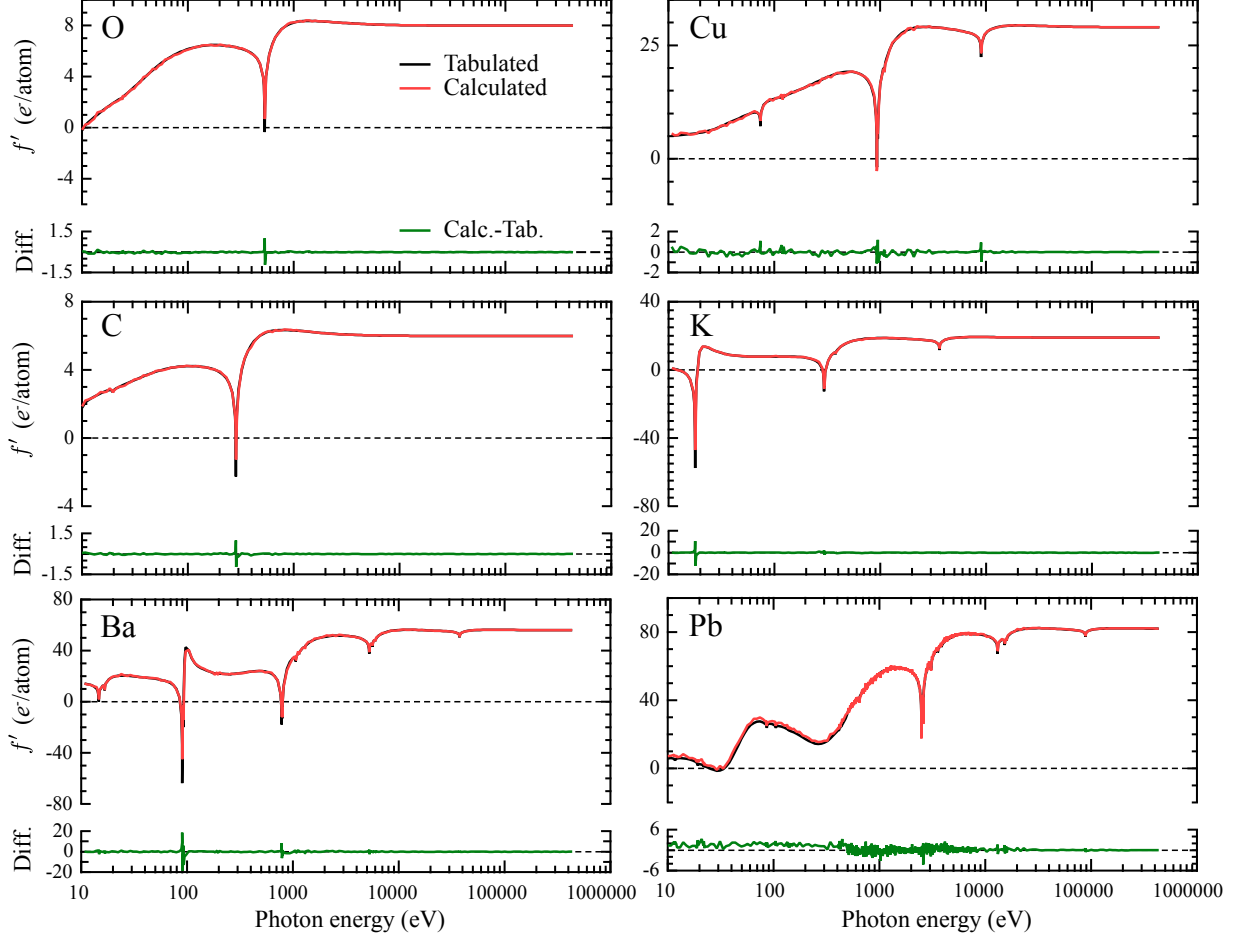


Figure 1.2 – The real part of $f = f' + i f''$ for O, Cu, C, K, Ba, and Pb was calculated (red) and is compared to the tabulated values of f' (black) for free-atoms. Here, f' also includes the Thomson term f^T , which is approximately Z for low \mathbf{Q} . The numerical integration strategy used to evaluate the Kramers-Kronig transformation is described in the text. Minor convergence issues are noticeable at the edge-steps due to discontinuities in f'' there. The tabulated values of f' and f'' are from Refs. [39, 40], which are accessible online.[41]

While the existing methods and tabulated values are generally better and have been more thoroughly verified for free-atom calculations of f' than this approach, another important benefit of this method is that it is simple to build upon it to reliably calculate near-edge values of f' for non-free atoms with experimental x-ray absorption data as an

input. This is a tremendously useful tool for modelling resonant soft x-ray scattering, since the x-ray absorption cross-section is sensitive to the “true” electronic structure of a material and it is in many cases simple to measure at a synchrotron. In contrast, relying on a quantum mechanical formula akin to Eq. 1.17, requires the self-consistent determination of the ground state and all intermediate state wavefunctions that the core-electron can transition into, which for atoms in a crystal can quickly become a very complicated problem. This problem can be made tractable if one makes assumptions about the electronic structure and takes advantage of an existing software package to do the calculations (eg. CTM4XAS [49]). This is a great way to identify the origin of different features in x-ray absorption spectra. Yet, the calculations typically need to be validated against x-ray absorption data, so there is little benefit to using the calculations rather than XAS as an input to resonant scattering model calculations.

A general outline of how to use empirical x-ray absorption data along with the Kramers-Kronig numerical transformation method above is as follows (the calculations in Chapters ?? and ?? followed this procedure):

1. Convert XAS for element X in a multi-atom material to a form proportional to f''
 - (a) Normalize XAS to $\sigma_{\text{tot}}^{\text{abs}} = \sigma_X^{\text{abs}} + \sigma_{\text{other}}^{\text{abs}}$ and then subtract $\sigma_{\text{other}}^{\text{abs}}$, giving σ_X^{abs}
 - (b) Calculate $\sigma_X^{\text{abs}} \times E \propto f'' = f''_{\text{data}}$
 - (c) Normalize f''_{data} to the tabulated values f''_{tables}
2. Join f''_{data} and f''_{tables} together
3. Define a function f''_{interp} that linearly interpolates the values f''_{data} and f''_{tables}
4. Define f''_{interp} for energies outside the tabulated range as
 - (a) $f''_{\text{interp}}(E < E_{\min}) = f''(E_{\min})$
 - (b) $f''_{\text{interp}}(E > E_{\max}) = f''(E_{\max})(E/E_{\max})^{-2}$
5. Evaluate Eq. 1.28 using f''_{interp} in the integrand.
Modify NIntegrate strategy as needed.

With this approach, it is possible to fully determine the complex atomic scattering form factor for an element within a crystal structure that has a non-trivial electronic structure. Utilizing the polarization dependence of the x-ray absorption measurement, it is also possible to determine the individual elements of the more general scattering tensor to treat

scattering for a more complex system. Then, armed with some knowledge (or a reasonable guess) of how \hat{f} depends on site index j in Eq. 1.21, it is possible to calculate how the resonant scattering intensity should depend on photon energy, polarization and \mathbf{Q} . In this thesis, the photon energy dependence is studied for the cuprates $\text{La}_{1.475}\text{Nd}_{0.4}\text{Sr}_{0.125}\text{CuO}_4$ and $\text{YBa}_2\text{Cu}_3\text{O}_{6.75}$ in Chapters ?? and ??, respectively, and the polarization and \mathbf{Q} dependence are evaluated for $\text{La}_{1.875}\text{Ba}_{0.125}\text{CuO}_4$ and $\text{YBa}_2\text{Cu}_3\text{O}_{6.67}$ in Chapter ??.

1.2.4 The polarization dependence in REXS

The polarization vectors are, in addition to the scattering tensor, an essential part of Eq. 1.21. They effectively provide sensitivity to the different elements of \hat{f} . In Eq. 1.21, ϵ and ϵ' are labeled explicitly with an index μ (although it is often omitted for brevity), which denotes the mode. These modes can be represented by two basis vectors which are perpendicular to the wave propagation direction. The convention is to define the basis with two linear polarization vectors ϵ_σ and ϵ_π , where ϵ_σ is perpendicular to the scattering plane and ϵ_π is parallel to it. One choice of basis that has its primary axes aligned with \mathbf{Q} , $\mathbf{k} + \mathbf{k}'$, and $\mathbf{k} \times \mathbf{k}'$ is depicted in Fig. 1.3.

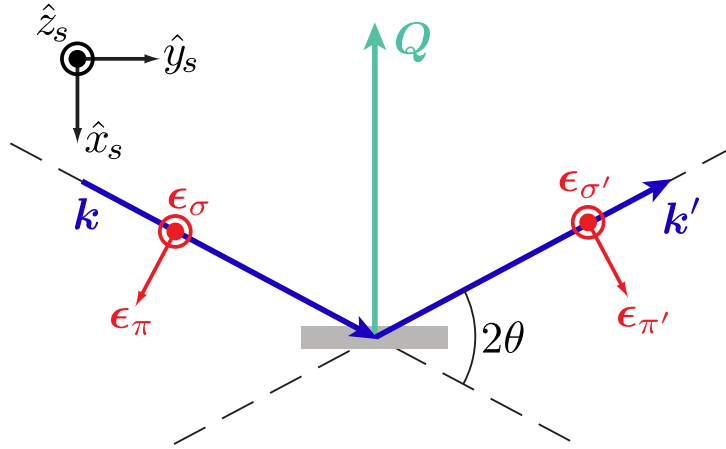


Figure 1.3 – Scattering geometry with reference frame chosen such that $\hat{x}_s \parallel (\mathbf{k} - \mathbf{k}')$, $\hat{y}_s \parallel (\mathbf{k} + \mathbf{k}')$, and $\hat{z}_s \parallel (\mathbf{k} \times \mathbf{k}')$. The angle between \mathbf{k} and \mathbf{k}' is defined as 2θ .

Formally, evaluation of Eq. 1.21 then requires summation over $\mu = \{\sigma, \pi\}$ and $\mu' = \{\sigma', \pi'\}$. There are four possibilities: $\sigma\sigma'$, $\sigma\pi'$, $\pi\sigma'$, and $\pi\pi'$. This can be represented as a

scattering matrix G (still at site j), given by

$$G_j = \begin{pmatrix} \epsilon_{\sigma'}^{*\dagger} \cdot \hat{f}_j \cdot \epsilon_\sigma & \epsilon_{\pi'}^{*\dagger} \cdot \hat{f}_j \cdot \epsilon_\sigma \\ \epsilon_{\sigma'}^{*\dagger} \cdot \hat{f}_j \cdot \epsilon_\pi & \epsilon_{\pi'}^{*\dagger} \cdot \hat{f}_j \cdot \epsilon_\pi \end{pmatrix}. \quad (1.30)$$

The scattering intensity is then $I \propto \left| \sum_{\mu, \mu'} \sum_j G_j e^{i\mathbf{Q} \cdot \mathbf{r}_j} \right|^2 = I_{\sigma\sigma'} + I_{\sigma\pi'} + I_{\pi\sigma'} + I_{\pi\pi'}$. Depending on the incident polarization and whether the polarization of the scattered rays can be discriminated, G can take on different forms. For example, if the incident light is σ or π polarized and an instrument is available to detect the outgoing light polarization, each scattering channel can be measured individually. More commonly (for soft x-ray beamlines), the incident polarization can be controlled but the outgoing polarization is unknown, leading to scattering that is either $I_{\sigma\sigma'} + I_{\sigma\pi'}$ or $I_{\pi\sigma'} + I_{\pi\pi'}$.

The case of Thomson scattering is particularly simple. For a spherically symmetric scatterer, we have $\hat{f}_j \propto I_3$, (I_3 is the identity matrix). With polarization vectors defined as in Fig. 1.3

$$\epsilon_\sigma = \begin{pmatrix} 0 \\ 0 \\ 1 \end{pmatrix} \quad \epsilon_{\sigma'} = \begin{pmatrix} 0 \\ 0 \\ 1 \end{pmatrix} \quad (1.31)$$

$$\epsilon_\pi = \begin{pmatrix} \cos \theta \\ -\sin \theta \\ 0 \end{pmatrix} \quad \epsilon_{\pi'} = \begin{pmatrix} \cos \theta \\ \sin \theta \\ 0 \end{pmatrix}, \quad (1.32)$$

we find

$$G = \begin{pmatrix} 1 & 0 \\ 0 & \cos(2\theta) \end{pmatrix}, \quad (1.33)$$

by evaluation of Eq. 1.30. This reveals that only the $\sigma \rightarrow \sigma'$ and $\pi \rightarrow \pi'$ scattering channels are active for Thomson scattering. If the incident light is σ polarized, then $I_\sigma^T = |f^T(\mathbf{Q})|^2$. For π polarization, we have $I_\pi^T = \cos^2(2\theta) |f^T(\mathbf{Q})|^2$. For unpolarized incident light, the scattering intensity is the average $I_{\text{unpol.}}^T = (1/2)(1 + \cos^2(2\theta)) |f^T(\mathbf{Q})|^2$. This pre-factor is the well-known polarization factor for Thomson scattering. Notably, for unpolarized incident incident light, Thomson scattering produces polarized light.

For non-magnetic charge scattering, the scattering tensor \hat{f}_{charge} (see Eq. 1.23) can be used, giving

$$G_{\text{charge}} = \begin{pmatrix} f_{zz} & 0 \\ 0 & f_{xx} \cos^2(\theta) - f_{yy} \sin^2(\theta) \end{pmatrix}. \quad (1.34)$$

Similar to Thomson scattering, charge scattering only consists of $\sigma \rightarrow \sigma'$ and $\pi \rightarrow \pi'$ processes. This relation can be useful when comparing resonant scattering intensities for incident σ or π polarization, although generally one also needs to take the absorption of the incident and scattered photons into account, since for an anisotropic absorption/scattering tensor the absorption cross-section would differ for σ and π polarization.

1.3 Experimental methods

1.3.1 Beamline

The RSXS experiments presented in this thesis date back to early 2010,⁷ and were all performed at the Canadian Light Source's REIXS (Resonant Elastic and Inelastic X-ray Scattering) 10ID-2 beamline using an in-vacuum four-circle diffractometer.[50] In synchrotron parlance, the REIXS beamline is referred to as 10ID-2, meaning that the insertion device (ID) is the second one installed on the 10th straight section of the CLS's storage ring. The ID at REIXS is an elliptically polarizing undulator (EPU) with 43 poles having a 75 mm period and spanning 1.6 m. This EPU produces linearly polarized photons with energy 100 → 3000 eV or circularly polarized (left or right) photons with energy 100 → 1000 eV. For linear polarization, the angle of the polarization can be set arbitrarily.

The optical configuration of the REIXS beamline is shown schematically in Fig. 1.4. REIXS features a variable line spacing plane grating monochromator (VLS-PGM) with three gratings (Ni low energy, Au low energy, Au high energy) and four coatings (Ni, C, Si, Au) on the plane mirror. These can be chosen to optimize flux at photon energies spanning the full energy range of the beamline. A variable exit slit can be used to adjust energy resolution, giving maximal energy resolutions of 0.005 eV at 100 eV and 0.13 eV at 1000 eV. The size of the exit slit gap is typically set in the 10–50 μm range and is approximately proportional to flux. The beamline produces a flux of 5×10^{12} photons/s/0.1% bandwidth (for 100 mA ring current and 1000 eV). Since the incident flux I_0 depends on energy,

⁷Specifically, the data presented here was collected from February 2010 to January 2015, beginning shortly after the REIXS beamline and scattering endstation were put together. For context, the monochromator and EPU at REIXS were installed in November and December of 2007, respectively, and two years later the scattering chamber received its first light (June 2009) and the first spectrum was recorded (July 2009). The diffractometer was commissioned (characterization and testing) from August 2009 to April 2010 by many people, including myself. Some of this early work is presented in Chapter ???. The first access to general users was later made possible by letters of intent (specific proposals likely to succeed) in May 2010, followed soon thereafter by competitive proposals (January 2011).

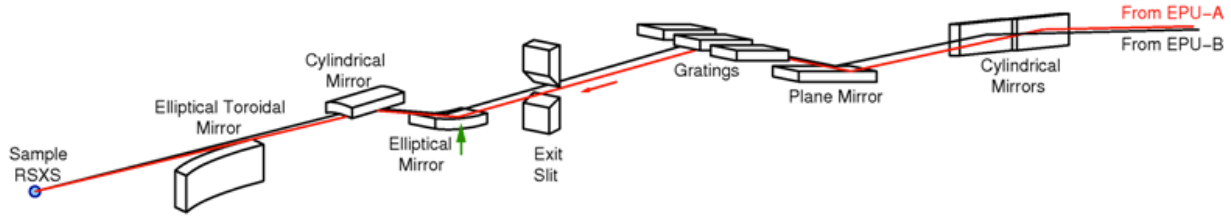


Figure 1.4 – Schematic of REIXS beamline showing novel x-ray optics configuration capable of sending spatially separated beams from two EPUs to the sample position simultaneously. Figure adapted from Ref. [51].

storage ring current and other beamline settings (grating, coating, exit slit gap, etc.), the electron yield from a high transmission Au mesh is used to record I_0 for normalization. The beam spot size at the sample position is width \times height $\approx 250 \times 150 \mu\text{m}$. Note that in typical usage, light from only one of two EPUs is sent down the optical path for scattering, but that REIXS features an operating mode and optics capable of using the light from 10ID-1 (normally servicing the neighbouring soft x-ray spectromicroscopy beamline) and 10ID-2 simultaneously, such that two different light polarizations can be rapidly switched during a measurement.

The entire beamline is operated in ultra-high vacuum (UHV) conditions ($P < 10^{-9}$ Torr). This is firstly needed to ensure a long lifetime of the electron orbit in the storage ring, which the EPU is a part of. It is also quite important due to the use of soft x-rays, since even for modest pressures, the mean path length of soft x-rays can suffer dramatically.⁸ Operating in UHV also reduces the amount of contaminants that can build up on optical elements of the beamline by limiting adsorption or potential condensation of gases such as water vapour onto these components. For samples that are heated and cooled in vacuum, this can also be quite important since certain measurements (e.g., electron yield or resonant reflectivity) can be sensitive to the topmost layers of the sample.

1.3.2 Diffractometer and detectors

The following discussion is an abbreviated summary of some of the essential aspects of the elastic scattering chamber and diffractometer design, which are covered thoroughly in Ref.

⁸See [Section A.3](#) for a brief illustration of this point.

[50]. Some details here will differ due to modifications to the system that have occurred since Ref. [50] was published in July 2011.

The ~ 1 m diameter stainless steel vacuum chamber pictured in Fig. 1.5 at the REIXS beamline houses an UHV 4-circle diffractometer (Fig. 1.6) consisting of a 2-circle goniometer mounted on a central θ ring and a detector arm mounted on a separate 2θ ring. The diffractometer is mounted on a separate subframe than the main scattering chamber and connected to it with flexible bellows, so that the diffractometer can be translated into the x-ray beam path independent of the main scattering chamber.

A load lock is used so samples can be transferred without venting the scattering chamber. The load lock has a garage for storage of up to 3 sample holders at a time. Sample holders are transferred into the scattering chamber using a magnetically coupled rack and pinion linear translator that uses a pincer mechanism to securely hold onto a small tab

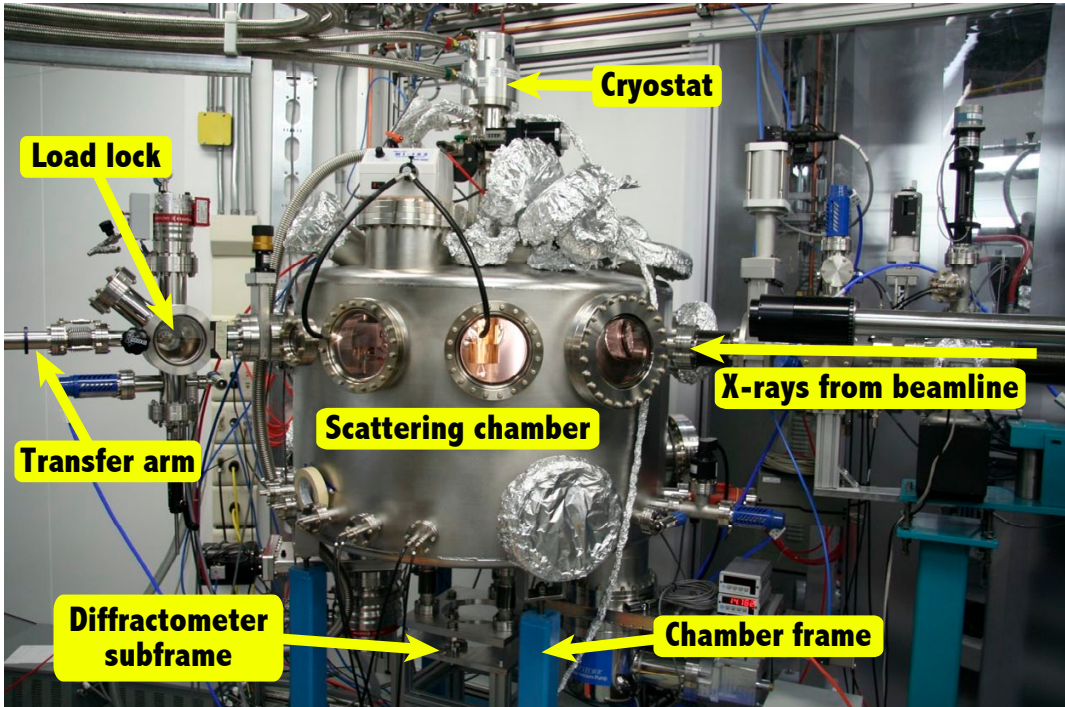


Figure 1.5 – The RSXS scattering chamber at the CLS’s REIXS beamline. A polarized, monochromatic beam of soft x-rays from the beamline enter from the right and focus at the sample position, centred in the scattering chamber. A load lock is used to store samples and facilitate sample transfers. The closed-cycle cryostat is mounted on top of the scattering chamber.

on the sample holder. Gate valves are used to isolate the scattering chamber from the beamline and the load lock from the scattering chamber during sample transfers.

The load lock is pumped down with a 300 L/s Pfeiffer turbopump and typically reaches 5×10^{-7} Torr in ~ 45 min or less, sufficiently low for transfers. The main chamber is pumped using a 700 L/s Pfeiffer turbopump (backed by a triscroll roughing pump) and a CTI Cryotorr 8F cryopump. A closed-cycle cryostat is mounted on a differentially pumped rotatory feedthrough, located at the top of the chamber. The feedthrough is pumped in two stages by the triscroll pump and a 2 L/s ion pump. The pressure in the scattering chamber is usually better than 5×10^{-9} Torr. Pressure gauges include a cold cathode gauge, a hot filament ion gauge and a residual gas analyzer, for low pressure measurements, as well as thermocouple and convection gauges for intermediate and high pressures, respectively.

Sample translations up to ± 7.5 mm are accomplished with stacked x, y and z linear translation stages mounted on the goniometer. The θ and 2θ motions, originally supported motion ranges of -25° to $+265^\circ$, but due to instrument modifications and practical considerations, ranges of -60° to 165° for θ and -25° to 172° for 2θ are currently imposed. The ϕ and χ motions have (approximate) ranges of $\pm 7^\circ$. These motions are primarily used to correct sample alignment but can also be used to expand the range of accessible \mathbf{Q} .

Cooling is achieved by connecting the cryostat's cold head to the sample receptacle with flexible copper braids (not seen in Fig. 1.6 since the braids are inside the heat shield). These braids damp vibrations from the cryostat and also reduce torsional forces if the cryostat

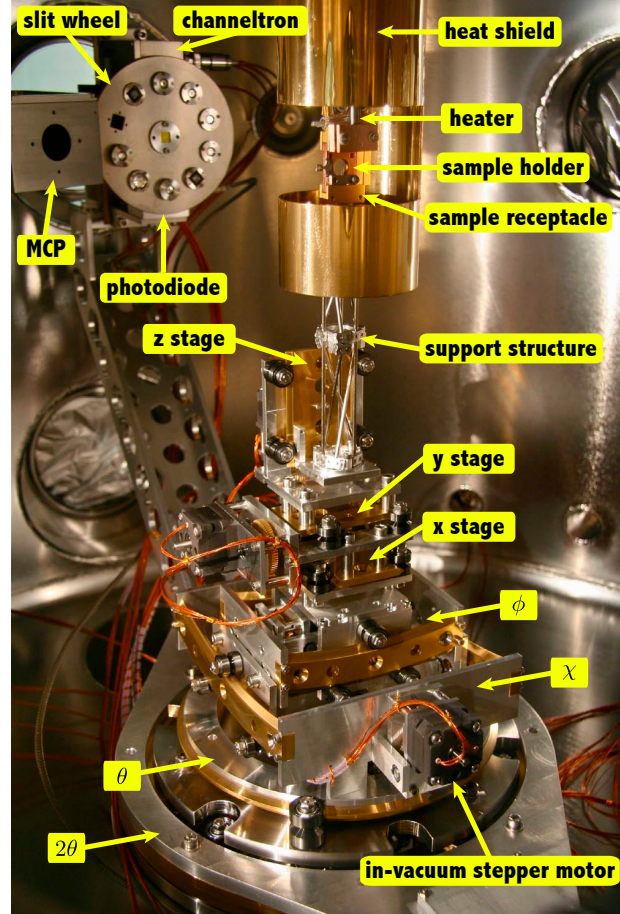


Figure 1.6 – The in-vacuum four-circle diffractometer at the CLS's REIXS beamline.

is stationary while θ is rotated (the cryostat can also be rotated to match θ rotations, keeping constant torsion on the support frame). Moreover, because the cooling elements are decoupled from the sample receptacle, their thermal expansion or contraction do not affect the sample position.

The sample receptacle is attached to a support structure, built with thin-walled stainless steel tubing, and mounted atop the translation stages of the goniometer. The support structure design minimizes thermal conduction between the sample holder (and receptacle) and the rest of the goniometer, reducing the heat load on the cryostat. It also limits thermal expansion of the support structure as the sample temperature is varied. For example, raising the temperature from 20 K to 298 K, thermal expansion accounts for just $\sim 180 \mu\text{m}$ of sample displacement along the z-axis, as shown in Fig. 1.7.

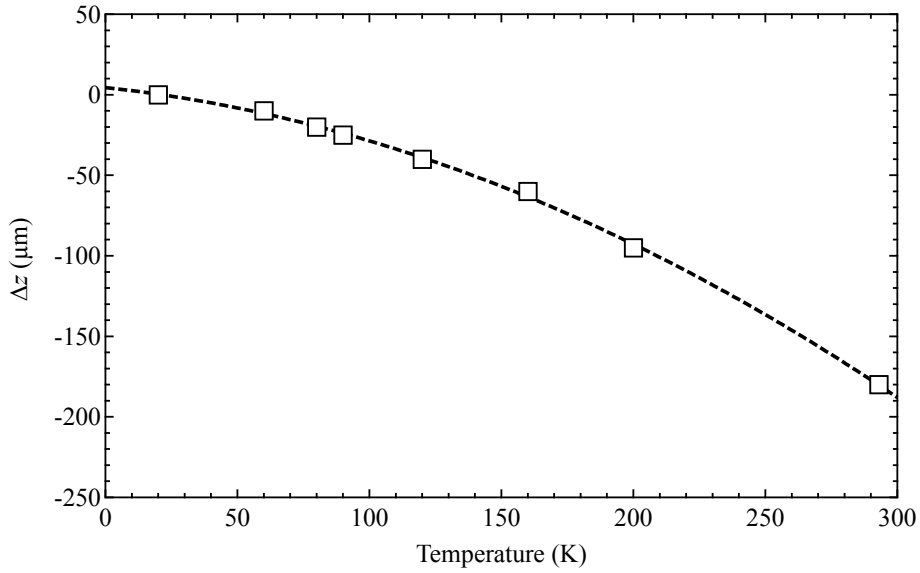


Figure 1.7 – The relative displacement $\Delta z = z(T) - z(20 \text{ K})$ due to thermal expansion of the support structure, sample holder, and sample receptacle. The negative sign indicates that the z stage must be lowered to centre as temperature is increased. The dashed line is a polynomial fit providing a reasonable interpolation scheme for this temperature range.

With the configuration pictured in Fig. 1.6, a base temperature at the sample position of 18 K was possible during the 2009 to October 2013 timeframe. At the end of 2013 (October to November) a magnet assembly was installed on the sample receptacle, increasing the thermal load and raising the base temperature to $\sim 23 \text{ K}$. This base temperature may

be improved in the future with planned revisions to the heatshield design. Heating is accomplished with a 100 W Lakeshore HTR-25-1000 cartridge heater, which is thermally connected to the sample receptacle just above the sample holder position. A sapphire plate and ceramic hat washers are used to electrically isolate the heater from the sample holder assembly. The heater is sufficiently powerful to raise the sample temperature to 400 K with the cryostat in operation.

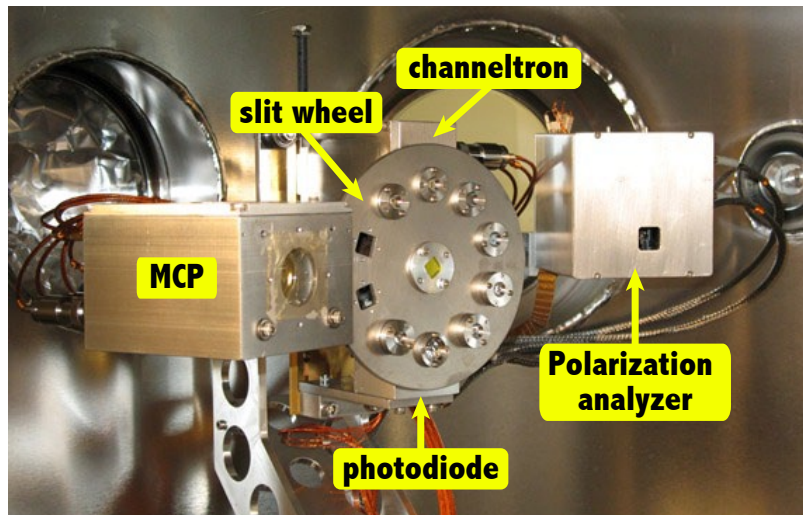


Figure 1.8 – Detector assembly in the RSXS scattering chamber

Four detectors are currently installed on the detector arm (Fig. 1.8): a micro-channel plate (MCP), a photodiode (PD), a channeltron (ChT) and a polarization analyzer. These are located at a radius of ~ 29 cm from the sample position and are mounted to a structure that can be raised or lowered by 40 mm to place any of the detectors in the scattering plane. The MCP has a 25 mm diameter and provides 2D sensitive single-photon detection capability. A negatively charged grid is placed in front the MCP to capture positively charged ions (from ion gauges or possibly ejected from the sample). The front surface is also negatively biased to repel electrons from the surface. The ChT is a 10×10 mm detector that provides single photon sensitivity similar to the MCP but without 2D sensitivity. It has a similar biasing scheme as the MCP. The PD has a 10×10 mm active area, is sensitive to a very wide range of photon energies with a linear response for photon energies up to 5 keV and a high dynamic range (currents can range from 10^{-12} to 10^{-5} A, suitable for the high flux of the direct beam or an x-ray fluorescence measurement). A slit wheel allows the selection of different slits (with width \times height of 10×10 mm, 1×2 mm, 0.5×3 mm).

mm, 0.1×3 mm, or 0.1×1 mm) and thin Al or SiN filters to be placed in front of either the ChT or PD. The different slits give control over detector resolution and the filters can be used to block charged ions or reduce the detection of background fluorescence.

The polarization analyzer uses two PDs and a selection of 4 multilayers suited for different x-ray absorption edges (O *K*: 530 eV, Mn *L*: 645 eV, Ni *L*: 860 eV, and Cu *L*: 940 eV), which can be switched using two Attocube rotary actuators, to reflect the vertical and horizontal polarization components of the scattered light into one of the two PDs. This design is not well suited to studying weak scattering signatures (as seen in this thesis), since the intensity losses due to this multilayer reflectivity are extreme (97% for O *K* and 99.85% for Cu *L*), but it can be useful in reflectivity experiments, where at small angles the flux of scattered light can be very high.

1.3.3 Sample preparation

For successful RSXS experiments, it is essential to prepare samples with good surface quality and with an orientation that provides access to a chosen zone in reciprocal space. This is because, unlike hard x-ray scattering, the range of \mathbf{Q} is very restricted and RSXS can be sensitive to surface effects. I will first discuss crystal orientation by Laue diffraction and then discuss crystal cleaving and polishing methods. Also, I will briefly describe the methods used to mount samples for RSXS measurements.

In many cases, the crystallographic orientation of as-grown crystals is not known. It is possible to determine the orientation with Laue diffraction. A typical configuration for Laue diffraction uses an x-ray tube with a tungsten target in order to produce a broad spectrum of x-rays. This broad spectrum of light can then readily satisfy Bragg's law (or the Laue condition) simultaneously for many crystal planes with different d_{hkl} and lead to a series of spots that can be recorded by photographic film. Laue diffraction can be measured in transmission (x-rays pass through a sample) or backscattering (x-rays are diffracted back towards x-ray tube) geometry. For the thick crystals studied in this thesis, backscattering geometry was more suitable. The backscattering geometry is depicted in Fig. 1.9.

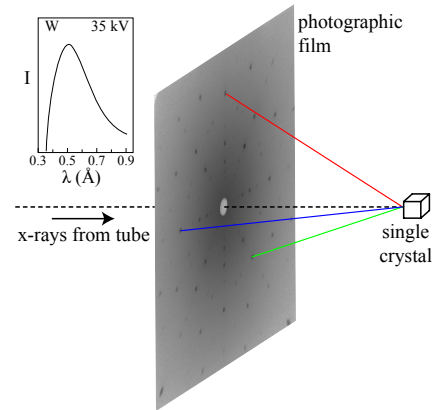


Figure 1.9 – Laue backscattering geometry for single crystal orientation.

A practical application is illustrated in Fig. 1.10. Here, Laue backscattering was used to orient an $\text{La}_{1.475}\text{Nd}_{0.4}\text{Sr}_{0.125}\text{CuO}_4$ (LNSCO) crystal boule with unknown orientation. First, a measurement on a cut surface was taken (left panels, Fig. 1.10). The orientation was solved using OrientExpress by indexing high symmetry points shown in the lower left panel of Fig. 1.10.[52] Angular corrections were calculated to orient the boule with the $a(b)$ axis perpendicular to the page and with c horizontal. A goniometer (see Fig. 1.11) was used to make these rotations and a subsequent Laue image (right panels, Fig. 1.10) confirmed the re-orientation.

The boule and goniometer were then transferred to a wire saw so that a cut could be made along the ab plane. The sample was then mounted on this flat surface so that subsequent cuts would produce tall samples with the c axis along the long side and a or b

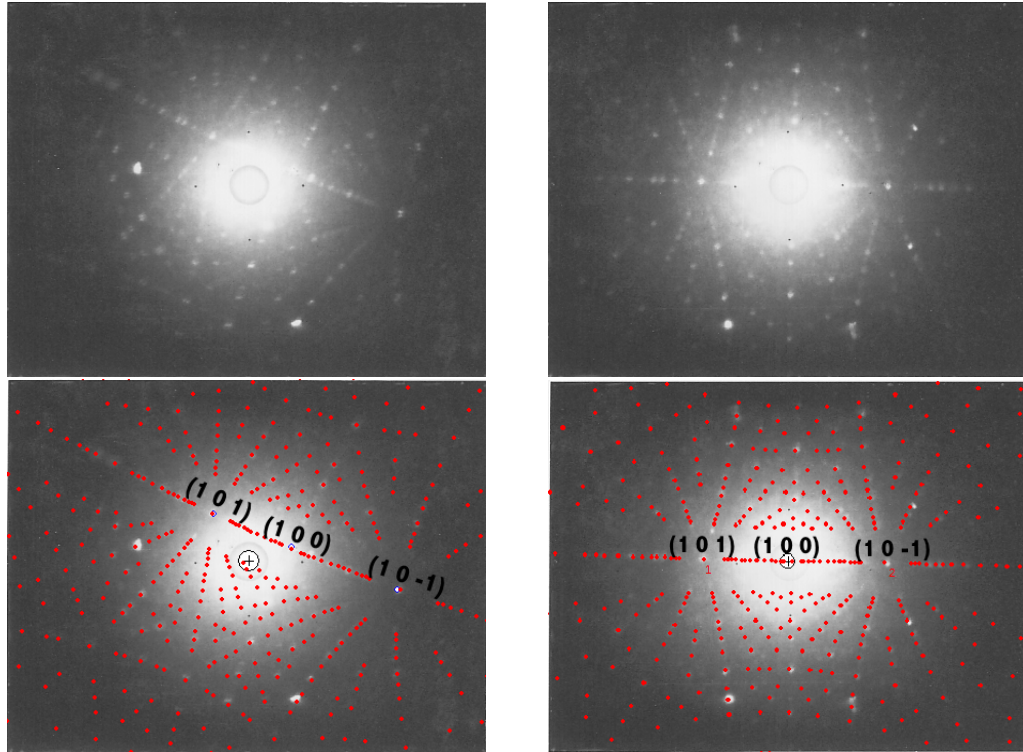


Figure 1.10 – Laue backscattering images taken on a cut surface of an LNSCO boule before (left) and after (right) orienting. The top row shows the Laue image as captured and the bottom row shows a superimposed Laue simulation obtained using OrientExpress.[52] (Simulation parameters: film to crystal distance: 35 mm, scattering geometry: 180° , space group: I4/mmm, lattice constants: $a=b=3.787 \text{ \AA}$, $c=13.24 \text{ \AA}$)

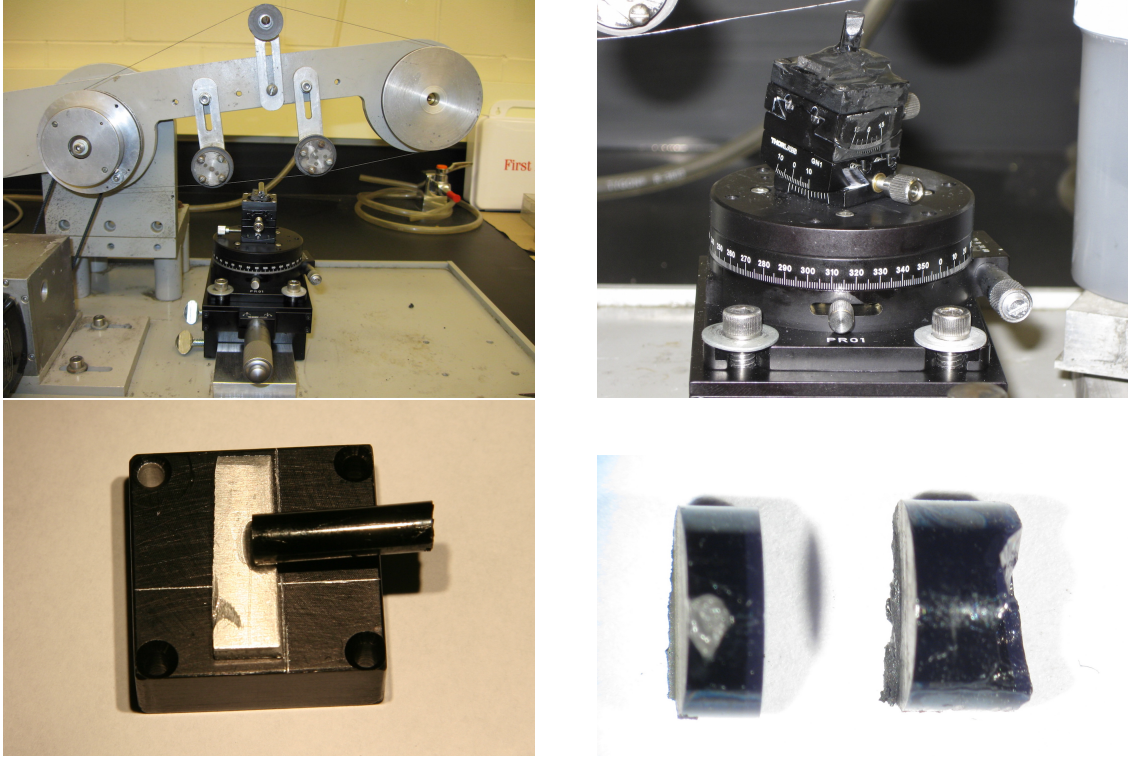


Figure 1.11 – A crystal boule of LNSCO was cut on a wire saw, first to expose a surface for Laue diffraction (top left), and then along a crystallographic plane (top right), for subsequent mounting (bottom left) and additional cuts (bottom right). The samples shown in the bottom right have the c axis out of the page and $a(b)$ along their width and length.

horizontal. The different cutting stages are illustrated in Fig. 1.11. These smaller pieces were then cut parallel to the flat edge,⁹ and finally once more along the horizontal of this page, producing 4 tall samples with approximately square bases and dimensions in the range of $\sim 1.5 \times 1.5 \times 3$ mm to $\sim 2 \times 2 \times 3$ mm.

After orienting a crystal, the next important consideration is the condition of the surface. The wire saw achieves its cutting action by dragging a grit of boron carbide across the sample, producing a rough and highly textured surface, as shown in Fig. 1.12 (a), not

⁹The flat edge enables further Laue measurements to establish the *final* orientation of the crystal, as-mounted and ready for scattering. This is important, since small errors compound and it is rare to have a perfectly oriented crystal. Knowing approximately where to look in angle-space with the soft x-ray diffractometer can save a lot of time.

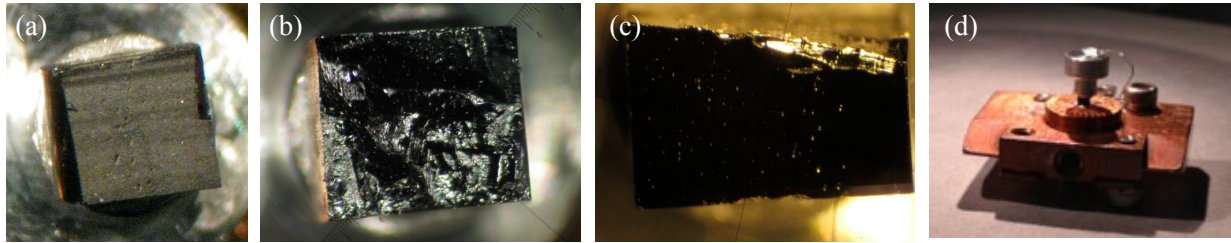


Figure 1.12 – (a)-(c) A sample of LNSCO with different surface conditions. (a) The rough surface results from cutting on the wire saw. (b) The shiny, bumpy surface results from fracturing in vacuum. (c) The flat, smooth, and shiny surface results from polishing (a piece broke off, giving it a trapezoidal shape). (d) An $\text{La}_{1.875}\text{Ba}_{0.125}\text{CuO}_4$ sample prepared for cleaving with a top post.

suitable for RSXS or XAS (due to surface damage and contamination). The load lock of the scattering chamber is equipped with a blade and anvil sample cleaver, which in this case was used to apply pressure to the sides of the sample and cause it to fracture in vacuum, producing a fresh surface [Fig. 1.12 (b)] for XAS and RSXS measurements.¹⁰ It is also possible to cleave or fracture a sample by attaching a post at the top of the sample [Fig. 1.12 (d)]. An impact is then delivered to the top post and if the crystal is weaker than its bonds to the sample plate and top post, a fresh surface will be exposed. Besides cleaving, one can also polish a crystal to produce a smooth, flat surface [Fig. 1.12 (c)].

Polishing was performed in stages usually beginning with a $10\ \mu\text{m}$ boron carbide powder, suspended in mineral oil, to obtain the primary grinding action. Water-based suspensions were avoided since cuprates are a bit hydroscopic. Using progressively finer powders (eg. “jeweler’s rouge”, ~ 0.5 to $1.5\ \mu\text{m}$), the surface could be smoothed down gradually. The finishing stages used 0.3 and $0.05\ \mu\text{m}$ lapping films. Given the delicate nature of the samples, this was all done by hand using a custom-built polishing assembly. The polishing direction could be aligned with a high-strength axis of the crystal to minimize the likelihood of fracturing. Despite this, parts of the samples did frequently fracture or break off (usually near the edges). A comparison of the surface conditions of two $\text{YBa}_2\text{Cu}_3\text{O}_{6+x}$ samples before and after polishing is shown in Fig. 1.13. The polished surfaces appeared smooth and mostly featureless at a magnification of $45\times$ (noted by eye, not pictured here).

For detecting charge density wave order by RSXS in La-based cuprates, cleaving samples has typically been a necessary step. Cleaving in vacuum or in air are both viable approaches, with the former having the benefit of giving more reliable electron yield at the

¹⁰The pictured sample is oriented with its weak plane not aligned with the sample cleaver, so the surface results formally from a fracture, not a cleave. The terms are often used interchangeably.

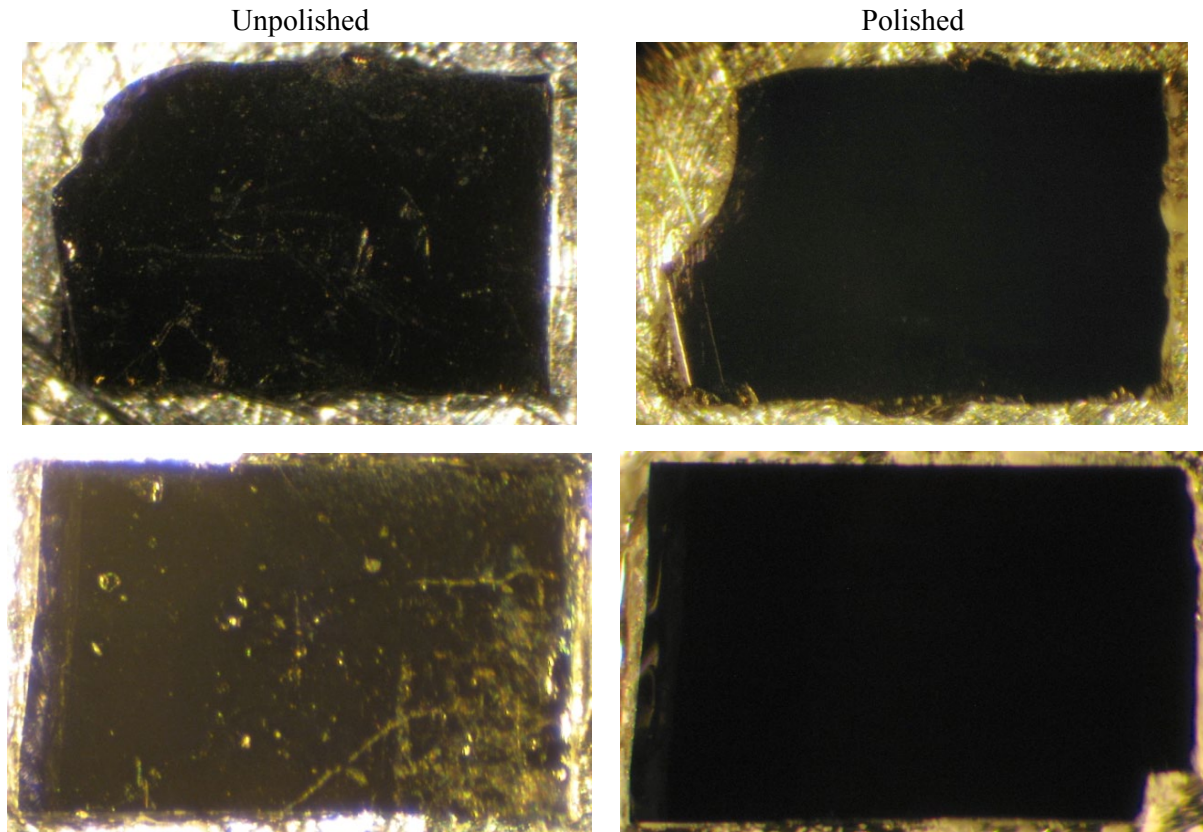


Figure 1.13 – Polishing $\text{YBa}_2\text{Cu}_3\text{O}_{6+x}$ samples. Left: unpolished samples. Right: after polishing. Polishing was performed in stages, as described in the text. The top row is a sample of $\text{YBa}_2\text{Cu}_3\text{O}_{6.335}$ and the bottom row is a sample of o-III ordered $\text{YBa}_2\text{Cu}_3\text{O}_{6.75}$. The polishing procedure succeeded in removing the surface imperfections. Although the polishing procedure was gentle, parts of both samples can be seen to have broken off.

expense of being a more difficult procedure. I have also had success detecting CDW order from a polished LNSCO surface. For $\text{YBa}_2\text{Cu}_3\text{O}_{6+x}$, polishing was useful for eliminating surface imperfections, but not essential for detecting the charge density wave order.

It is also important to have good electrical and thermal conductivity with the sample holder. Electrical contact can be made using silver epoxy (EPO-TEK H21D), high purity silver paint (SPI #5001-AB), silver paste (SPI #5063-AB) or carbon tape (SPI #05081-AB). For low temperatures or experiments with significant temperature cycling, the silver epoxy and paint are better choices, since they retain their strength and provide excellent

thermal and electrical conductivity. Silver epoxy forms a much stronger and more permanent bond than silver paint, making it suitable when samples are to be cleaved. Silver epoxy can be excessive for many applications, since removing it typically requires scraping with a scalpel and hours of sonication in acetone. In contrast, silver paint can be removed with a few minutes of sonication in acetone. For room temperature measurements, silver paste and carbon tape are good choices. Silver paste dissolves in acetone, with little need for sonication. Samples mounted on carbon tape can usually be removed simply with tweezers. Occasionally, carbon tape residue is left on the sample. The residue can be wiped off or dissolved in acetone.

APPENDICES

Appendix A

Useful formulae and calculations

A.1 Relation between Miller indices and $(\theta, 2\theta)$ in a 2-circle scattering geometry

We begin with the Laue equations written in Eq. 1.1. Recall that \mathbf{a}_1 , \mathbf{a}_2 and \mathbf{a}_3 are the primitive vectors of the crystal lattice and H , K and L are Miller indices for a reciprocal lattice vector \mathbf{G} that satisfies $\mathbf{G} = H\mathbf{b}_1 + K\mathbf{b}_2 + L\mathbf{b}_3$, where \mathbf{b}_1 , \mathbf{b}_2 and \mathbf{b}_3 are the basis vectors for the reciprocal lattice.[24]

$$\begin{aligned}\mathbf{a}_1 \cdot (\mathbf{k}' - \mathbf{k}) &= 2\pi H \\ \mathbf{a}_2 \cdot (\mathbf{k}' - \mathbf{k}) &= 2\pi K \\ \mathbf{a}_3 \cdot (\mathbf{k}' - \mathbf{k}) &= 2\pi L\end{aligned}\tag{A.1}$$

Working in the lab reference frame, rotations of the sample about the center of a four-circle diffractometer have the effect of rotating the primitive vectors. The rotation rotation matrix for our four-circle diffractometer that gives this rotation is $R = R_\theta \cdot R_\chi \cdot R_\phi$, written fully as:

$$R = \begin{pmatrix} \cos(\theta) \cos(\phi) - \sin(\theta) \sin(\chi) \sin(\phi) & -\sin(\theta) \cos(\chi) & \sin(\theta) \sin(\chi) \cos(\phi) + \cos(\theta) \sin(\phi) \\ \cos(\theta) \sin(\chi) \sin(\phi) + \sin(\theta) \cos(\phi) & \cos(\theta) \cos(\chi) & \sin(\theta) \sin(\phi) - \cos(\theta) \sin(\chi) \cos(\phi) \\ -\cos(\chi) \sin(\phi) & \sin(\chi) & \cos(\chi) \cos(\phi) \end{pmatrix}.\tag{A.2}$$

We define the beam direction as \hat{x} , the sample normal when $\theta = 0$ as \hat{y} , and the vertical direction as \hat{z} . This definition gives $\mathbf{k} = \frac{2\pi E}{hc} \hat{x}$ and $\mathbf{k}' = \frac{2\pi E}{hc} [\cos(\omega) \hat{x} + \sin(\omega) \hat{y}]$, where I am now using ω instead of 2θ to avoid confusing notation, E is the photon energy in eV, and hc is Planck's constant times the speed of light in vacuum.¹ Thus $\mathbf{Q} = \mathbf{k}' - \mathbf{k} = \frac{2\pi E}{hc} [(-1 + \cos(\omega)) \hat{x} + \sin(\omega) \hat{y}]$. For an orthorhombic crystal mounted with its a axis aligned to $-\hat{x}$, its b axis aligned to \hat{z} and its c axis aligned to \hat{y} (lattice constants a , b , and c), Eq. A.1 becomes

$$\begin{aligned}R \cdot (-\hat{x}) \cdot (\mathbf{k}' - \mathbf{k}) &= 2\pi H/a \\ R \cdot (+\hat{z}) \cdot (\mathbf{k}' - \mathbf{k}) &= 2\pi K/b \\ R \cdot (+\hat{y}) \cdot (\mathbf{k}' - \mathbf{k}) &= 2\pi L/c\end{aligned}\tag{A.3}$$

¹Note that when c appears as hc , it is the speed of the light, whereas when it appears as L/c , it is the lattice constant.

For a diffractometer operating in 2-circle mode, we can set χ and ϕ to 0, thus simplifying Eq. A.3 considerably. First, we find that $K = (0\ 0\ 1) \cdot (\mathbf{k}' - \mathbf{k}) = 0$, reducing the problem from 3 to 2 dimensions. The two remaining equations are then given by:

$$-\frac{hc}{E} \frac{H}{a} = \cos(\theta - \omega) - \cos(\theta) \quad (\text{A.4})$$

$$-\frac{hc}{E} \frac{L}{c} = \sin(\theta - \omega) - \sin(\theta). \quad (\text{A.5})$$

Dividing Eq. A.4 by Eq. A.5, we arrive at

$$\frac{H}{L} \frac{c}{a} = \tan\left(\frac{\omega}{2} - \theta\right). \quad (\text{A.6})$$

Adding the square of Eq. A.4 to the square of Eq. A.5, we arrive at

$$\left(\frac{hc}{E}\right)^2 \left(\frac{H^2}{a^2} + \frac{L^2}{c^2}\right) = 2 - 2\cos(\omega), \quad (\text{A.7})$$

which can be re-written using the trigonometric identity $2 - 2\cos(x) = 4\sin^2(x/2)$ and taking the square root of both sides

$$\frac{hc}{2E} \sqrt{\frac{H^2}{a^2} + \frac{L^2}{c^2}} = \sin\left(\frac{\omega}{2}\right). \quad (\text{A.8})$$

Eq. A.8 is just a 2-dimensional formulation of Bragg's Law, $n\lambda = 2d\sin(\theta_B)$. We can see this by using the relations $\lambda = \frac{hc}{E}$, $\sqrt{\frac{H^2}{a^2} + \frac{L^2}{c^2}} = \frac{1}{d}$, $n = 1$, and $\sin(\frac{\omega}{2}) = \sin(\theta_B)$.

The equations Eq. A.6 and Eq. A.8 can be used to solve for (θ, ω) for a desired (H, L) . This is how Eq. 1.2 and Eq. 1.3 were derived in the main text. Note, a different notation was used ($\omega \rightarrow 2\theta$, $\theta \rightarrow \theta_s$, $L \rightarrow K$, $c \rightarrow b$). Explicitly, in this notation, the relations are:

$$\omega = 2\sin^{-1} \left(\frac{hc}{2E} \sqrt{\left(\frac{H}{a}\right)^2 + \left(\frac{L}{c}\right)^2} \right) \quad (\text{A.9})$$

$$\theta = \frac{\omega}{2} - \tan^{-1} \left(\frac{H}{L} \frac{c}{a} \right), \quad (\text{A.10})$$

Interestingly, when deriving Bragg's Law from the Laue equations, we realize that Bragg's Law fails to relate θ to the Miller indices. For any Bragg peak with $H = 0$, this does not matter, as we have a specular condition and $\theta = \omega/2$ by definition. It also does not matter for measurements of crystalline powders (with all possible orientations fulfilled), as then the definition of θ is meaningless. For diffraction from single crystals, however, one certainly needs to use the Laue formulation!

A.2 Wedge angle for azimuthal rotation experiment

In chapter ?? an azimuthal rotation experiment was performed to rotate sample about \mathbf{Q}_{CDW} . For this a wedge-shaped azimuthal sample plug had to be made with the correct surface angle. See Fig. ?? for the geometry. Here I will derive the formula for this angle.

The wedge acts as an additional rotation that occurs before ϕ , χ or θ , so the rotation matrix with the wedge included is given by $R = R_\theta \cdot R_\chi \cdot R_\phi \cdot R_w$, where R_w will provide a rotation about the \hat{z} axis in the positive θ direction of magnitude θ_w . This can be simplified using the substitutions $\theta = \omega/2$ and $\chi = 0$. The former ensures that the axis of rotation of ϕ is aligned with \mathbf{Q} (specular geometry with $\theta_w = 0$), while the latter limits the possible solutions to those only involving θ_w . The rotation matrix is then given by:

$$R = \begin{pmatrix} \cos(w) \cos\left(\frac{\omega}{2}\right) \cos(\phi) - \sin(w) \sin\left(\frac{\omega}{2}\right) & -\sin(w) \cos\left(\frac{\omega}{2}\right) \cos(\phi) - \cos(w) \sin\left(\frac{\omega}{2}\right) & \cos\left(\frac{\omega}{2}\right) \sin(\phi) \\ \sin(w) \cos\left(\frac{\omega}{2}\right) + \cos(w) \sin\left(\frac{\omega}{2}\right) \cos(\phi) & \cos(w) \cos\left(\frac{\omega}{2}\right) - \sin(w) \sin\left(\frac{\omega}{2}\right) \cos(\phi) & \sin\left(\frac{\omega}{2}\right) \sin(\phi) \\ -\cos(w) \sin(\phi) & \sin(w) \sin(\phi) & \cos(\phi) \end{pmatrix}. \quad (\text{A.11})$$

We then evaluate the system Eq. A.3 using Eq. A.11 and find that it reduces to

$$\begin{aligned} -\frac{H}{a} &= 2 \sin(\theta_w) \sin\left(\frac{\omega}{2}\right) \frac{E}{hc} \\ \frac{K}{b} &= 0 \\ \frac{L}{c} &= 2 \cos(\theta_w) \sin\left(\frac{\omega}{2}\right) \frac{E}{hc} \end{aligned} \quad (\text{A.12})$$

The wedge angle is thus found easily, giving

$$\theta_w = -\tan^{-1}\left(\frac{H}{L} \frac{c}{a}\right). \quad (\text{A.13})$$

The sign is not important for manufacturing the wedge. However, some care should be taken when defining $\phi = 0$ in this system. Whether the wedge angle adds to θ or subtracts from θ at $\phi = 0$ turns out to be important for comparison to model calculations that incorporate absorption effects, since these can cause the scattering intensity for $\phi = 0^\circ$ and $\phi = 180^\circ$ to differ.

A.3 Photon path lengths

The maximum path length p_{\max} (cm) that photons of energy E can traverse through air while retaining a fraction $f = I/I_0$ of their initial flux can be approximated by

$$p_{\max} = -\ln(f)(\rho\mu(E))^{-1}, \quad (\text{A.14})$$

where $\mu(E)$ is the x-ray attenuation coefficient (cm^2/g) and $\rho = 4.64444 \times 10^{-4}P/T$ is the density of dry air (g/cm^3) with pressure P (Torr) and temperature T (K). Table A.1 shows p_{\max} for 100 eV photons passing through dry air at room temperature calculated at pressures ranging from atmospheric pressure to UHV. Note that higher energy photons have larger p_{\max} than calculated here, since $\mu(100 \text{ eV}) > \mu(E > 100 \text{ eV})$ for dry air.

Table A.1: Maximum path length p_{\max} that 100 eV photons can traverse through dry air while maintaining $I/I_0 > f$ as a function of pressure. Calculated for $T = 20^\circ\text{C}$.

P (Torr)	p_{\max} (cm)	p_{\max} (cm)
	$f = 0.50$	$f = 0.99$
760	1.19×10^{-2}	1.72×10^{-4}
100	9.02×10^{-2}	1.31×10^{-3}
1	9.02	1.31×10^{-1}
10^{-3}	9.02×10^3	1.31×10^2
10^{-6}	9.02×10^6	1.31×10^5
10^{-9}	9.02×10^9	1.31×10^8

As a practical example, if we want to build a 20 m long beamline (at room temperature) and we want less than 1% flux loss for 100 eV photons, using Eq. A.14, we find that P must be less than 6.54×10^{-5} Torr. This illustrates one fundamental reason why soft x-ray beamlines typically operate in UHV conditions for all of their optical components. Other reasons are the need to be connected to the storage ring, which is kept under UHV, and to minimize contamination on optical components. The generally much smaller experimental endstations can in principle be designed to operate at higher pressures with consideration of these flux losses.

References

- [1] Vettier, C., Resonant elastic X-ray scattering: Where from? where to? *The European Physical Journal Special Topics* **208**, 3–14 (2012), DOI: [10.1140/epjst/e2012-01602-7](https://doi.org/10.1140/epjst/e2012-01602-7).
- [2] Sasaki, S., Analyses for a planar variably-polarizing undulator. *Nuclear Instruments and Methods in Physics Research Section A* **347**, 83–86 (1994), DOI: [10.1016/0168-9002\(94\)91859-7](https://doi.org/10.1016/0168-9002(94)91859-7).
- [3] Bilderback, D.H., Elleaume, P., & Weckert, E., Review of third and next generation synchrotron light sources. *Journal of Physics B: Atomic, Molecular and Optical Physics* **38**, S773–S797 (2005), DOI: [10.1088/0953-4075/38/9/022](https://doi.org/10.1088/0953-4075/38/9/022).
- [4] Templeton, D.H. & Templeton, L.K., X-ray dichroism and polarized anomalous scattering of the uranyl ion. *Acta Crystallographica Section A* **38**, 62–67 (1982), DOI: [10.1107/S0567739482000114](https://doi.org/10.1107/S0567739482000114).
- [5] Dmitrienko, V.E., Forbidden reflections due to anisotropic X-ray susceptibility of crystals. *Acta Crystallographica Section A* **39**, 29–35 (1983), DOI: [10.1107/S0108767383000057](https://doi.org/10.1107/S0108767383000057).
- [6] Blume, M. & Gibbs, D., Polarization dependence of magnetic x-ray scattering. *Phys. Rev. B* **37**, 1779–1789 (1988), DOI: [10.1103/PhysRevB.37.1779](https://doi.org/10.1103/PhysRevB.37.1779).
- [7] Hannon, J.P., Trammell, G.T., Blume, M., & Gibbs, D., X-Ray Resonance Exchange Scattering. *Phys. Rev. Lett.* **61**, 1245–1248 (1988), DOI: [10.1103/PhysRevLett.61.1245](https://doi.org/10.1103/PhysRevLett.61.1245).
- [8] Kotani, A. & Shin, S., Resonant inelastic x-ray scattering spectra for electrons in solids. *Rev. Mod. Phys.* **73**, 203–246 (2001), DOI: [10.1103/RevModPhys.73.203](https://doi.org/10.1103/RevModPhys.73.203).

- [9] Ament, L.J.P., van Veenendaal, M., Devereaux, T.P., Hill, J.P., & van den Brink, J., Resonant inelastic x-ray scattering studies of elementary excitations. *Rev. Mod. Phys.* **83**, 705–767 (2011), DOI: [10.1103/RevModPhys.83.705](https://doi.org/10.1103/RevModPhys.83.705).
- [10] Carra, P. & Thole, B.T., Anisotropic x-ray anomalous diffraction and forbidden reflections. *Rev. Mod. Phys.* **66**, 1509–1515 (1994), DOI: [10.1103/RevModPhys.66.1509](https://doi.org/10.1103/RevModPhys.66.1509).
- [11] Hill, J.P. & McMorrow, D.F., X-ray resonant exchange scattering: Polarization dependence and correlation functions. *Acta Crystallographica Section A* **52**, 236–244 (1996), DOI: [10.1107/S0108767395012670](https://doi.org/10.1107/S0108767395012670).
- [12] Lovesey, S., Balcar, E., Knight, K., & Rodríguez, J.F., Electronic properties of crystalline materials observed in X-ray diffraction. *Physics Reports* **411**, 233–289 (2005), DOI: [10.1016/j.physrep.2005.01.003](https://doi.org/10.1016/j.physrep.2005.01.003).
- [13] Dmitrienko, V.E., Ishida, K., Kirfel, A., & Ovchinnikova, E.N., Polarization anisotropy of X-ray atomic factors and ‘forbidden’ resonant reflections. *Acta Crystallographica Section A* **61**, 481–493 (2005), DOI: [10.1107/S0108767305018209](https://doi.org/10.1107/S0108767305018209).
- [14] Matteo, S.D., Resonant x-ray diffraction: multipole interpretation. *Journal of Physics D: Applied Physics* **45**, 163001 (2012), DOI: [10.1088/0022-3727/45/16/163001](https://doi.org/10.1088/0022-3727/45/16/163001).
- [15] Joly, Y., Matteo, S.D., & Bunău, O., Resonant X-ray diffraction: Basic theoretical principles. *The European Physical Journal Special Topics* **208**, 21–38 (2012), DOI: [10.1140/epjst/e2012-01604-5](https://doi.org/10.1140/epjst/e2012-01604-5).
- [16] Detlefs, C., Sanchez del Rio, M., & Mazzoli, C., X-ray polarization: General formalism and polarization analysis. *The European Physical Journal Special Topics* **208**, 359–371 (2012), DOI: [10.1140/epjst/e2012-01630-3](https://doi.org/10.1140/epjst/e2012-01630-3).
- [17] Fink, J., Schierle, E., Weschke, E., & Geck, J., Resonant elastic soft x-ray scattering. *Reports On Progress In Physics* **76**, 056502 (2013), DOI: [10.1088/0034-4885/76/5/056502](https://doi.org/10.1088/0034-4885/76/5/056502).
- [18] Hahn, T. (Editor), *International Tables for Crystallography*, Vol. A, Space-group symmetry, chapter 9 (Chester: International Union of Crystallography, 2006), first online edition, DOI: [10.1107/97809553602060000100](https://doi.org/10.1107/97809553602060000100).
- [19] Thomas, J.M., Centenary: The birth of X-ray crystallography. *Nature* **491**, 186–187 (2012), DOI: [10.1038/491186a](https://doi.org/10.1038/491186a).

- [20] Sumner, T., Dazzling History. *Science* **343**, 1092–1093 (2014), DOI: [10.1126/science.343.6175.1092](https://doi.org/10.1126/science.343.6175.1092).
- [21] Marder, M.P., *Scattering and Structures*, chapter 3, (pages 43–75) (John Wiley & Sons, Inc., 2010), ISBN 9780470949955, DOI: [10.1002/9780470949955.ch3](https://doi.org/10.1002/9780470949955.ch3).
- [22] Bragg, W.H. & Bragg, W.L., The Reflection of X-rays by Crystals. *Proceedings of the Royal Society of London A: Mathematical, Physical and Engineering Sciences* **88**, 428–438 (1913), DOI: [10.1098/rspa.1913.0040](https://doi.org/10.1098/rspa.1913.0040).
- [23] Friedrich, W., Knipping, P., & Laue, M., Interferenzerscheinungen bei Röntgenstrahlen. *Annalen der Physik* **346**, 971–988 (1913), DOI: [10.1002/andp.19133461004](https://doi.org/10.1002/andp.19133461004).
- [24] Prince, E. (Editor), *International Tables for Crystallography*, Vol. C, Mathematical, physical and chemical tables, chapter 1 (Chester: International Union of Crystallography, 2006), first online edition, DOI: [10.1107/97809553602060000103](https://doi.org/10.1107/97809553602060000103).
- [25] spec: Software for Diffraction, URL: <http://www.certif.com/content/spec/>.
- [26] Busing, W. & Levy, H., Angle calculations for 3-and 4-circle X-ray and neutron diffractometers. *Acta Crystallographica* **22**, 457–464 (1967), DOI: [10.1107/S0365110X67000970](https://doi.org/10.1107/S0365110X67000970).
- [27] Foldy, L.L., The Electromagnetic Properties of Dirac Particles. *Phys. Rev.* **87**, 688–693 (1952), DOI: [10.1103/PhysRev.87.688](https://doi.org/10.1103/PhysRev.87.688).
- [28] Jackson, J.D., *Classical Electrodynamics* (Wiley, 1998), third edition, ISBN 047130932X, URL: <http://www.worldcat.org/oclc/38073290>.
- [29] Altarelli, M., Resonant X-ray Scattering: A Theoretical Introduction. In *Magnetism: A Synchrotron Radiation Approach*, Vol. 697 of *Lecture Notes in Physics*, edited by E. Beaurepaire, H. Bulou, F. Scheurer, & J.P. Kappler, (pages 201–242) (Springer Berlin Heidelberg, 2006), ISBN 978-3-540-33241-1, DOI: [10.1007/3-540-33242-1_8](https://doi.org/10.1007/3-540-33242-1_8).
- [30] Sakurai, J.J., *Advanced Quantum Mechanics*, chapter 3, (pages 75–178) (Addison-Wesley, 1967), first edition, ISBN 0201067102, URL: <http://www.worldcat.org/oclc/869733>.
- [31] Dirac, P.A.M., The Quantum Theory of the Electron. *Proceedings of the Royal Society of London. Series A* **117**, 610–624 (1928), DOI: [10.1098/rspa.1928.0023](https://doi.org/10.1098/rspa.1928.0023).

- [32] Dirac, P.A.M., The Quantum Theory of the Emission and Absorption of Radiation. *Proceedings of the Royal Society of London. Series A* **114**, 243–265 (1927), DOI: [10.1098/rspa.1927.0039](https://doi.org/10.1098/rspa.1927.0039).
- [33] Sakurai, J.J., *Advanced Quantum Mechanics*, chapter 2, (pages 21–64) (Addison-Wesley, 1967), first edition, ISBN 0201067102, URL: <http://www.worldcat.org/oclc/869733>.
- [34] Blume, M., Magnetic scattering of x rays (invited). *Journal of Applied Physics* **57**, 3615–3618 (1985), DOI: [10.1063/1.335023](https://doi.org/10.1063/1.335023).
- [35] Lovesey, S. & Collins, S., *X-ray Scattering and Absorption by Magnetic Materials*. Oxford science publications (Clarendon Press, 1996), ISBN 9780198517375, URL: <http://www.worldcat.org/oclc/283724551>.
- [36] Collins, S. & Bombardi, A., Resonant X-Ray Scattering and Absorption. In *Magnetism and Synchrotron Radiation*, Vol. 133 of *Springer Proceedings in Physics*, edited by E. Beaurepaire, H. Bulou, F. Scheurer, & K. Jean-Paul, (pages 223–262) (Springer Berlin Heidelberg, 2010), ISBN 978-3-642-04498-4, DOI: [10.1007/978-3-642-04498-4_8](https://doi.org/10.1007/978-3-642-04498-4_8).
- [37] Wende, H. & Antoniak, C., X-Ray Magnetic Dichroism. In *Magnetism and Synchrotron Radiation*, Vol. 133 of *Springer Proceedings in Physics*, edited by E. Beaurepaire, H. Bulou, F. Scheurer, & K. Jean-Paul, (pages 145–167) (Springer Berlin Heidelberg, 2010), ISBN 978-3-642-04497-7, DOI: [10.1007/978-3-642-04498-4_5](https://doi.org/10.1007/978-3-642-04498-4_5).
- [38] Haverkort, M.W., Hollmann, N., Krug, I.P., & Tanaka, A., Symmetry analysis of magneto-optical effects: The case of x-ray diffraction and x-ray absorption at the transition metal $L_{2,3}$ edge. *Phys. Rev. B* **82**, 094403 (2010), DOI: [10.1103/PhysRevB.82.094403](https://doi.org/10.1103/PhysRevB.82.094403).
- [39] Chantler, C.T., Theoretical Form Factor, Attenuation, and Scattering Tabulation for $Z=1\text{--}92$ from $E=1\text{--}10$ eV to $E=0.4\text{--}1.0$ MeV. *J. Phys. Chem. Ref. Data* **24**, 71–643 (1995), DOI: [10.1063/1.555974](https://doi.org/10.1063/1.555974).
- [40] Chantler, C.T., Detailed Tabulation of Atomic Form Factors, Photoelectric Absorption and Scattering Cross Section, and Mass Attenuation Coefficients in the Vicinity of Absorption Edges in the Soft X-Ray ($Z=30\text{--}36$, $Z=60\text{--}89$, $E=0.1$ keV–10 keV), Addressing Convergence Issues of Earlier Work. *Journal of Physical and Chemical Reference Data* **29**, 597–1056 (2000), DOI: [10.1063/1.1321055](https://doi.org/10.1063/1.1321055).

- [41] National Institute of Standards and Technology: X-Ray Form Factor, Attenuation, and Scattering Tables, URL: <http://www.nist.gov/pml/data/ffast/index.cfm>.
- [42] Henke, B., Gullikson, E., & Davis, J., X-Ray Interactions: Photoabsorption, Scattering, Transmission, and Reflection at $E = 50\text{-}30,000 \text{ eV}$, $Z = 1\text{-}92$. *Atomic Data and Nuclear Data Tables* **54**, 181–342 (1993), DOI: [10.1006/adnd.1993.1013](https://doi.org/10.1006/adnd.1993.1013).
- [43] The Center for X-ray Optics: X-Ray Interactions With Matter, URL: http://henke.lbl.gov/optical_constants/.
- [44] Tabulated atomic scattering form factors and a Mathematica notebook to extract data, URL: https://github.com/AJAthesis/f1f2_AtomicDB.
- [45] Newton, R.G., Optical theorem and beyond. *American Journal of Physics* **44**, 639–642 (1976), DOI: [10.1119/1.10324](https://doi.org/10.1119/1.10324).
- [46] Toll, J.S., Causality and the Dispersion Relation: Logical Foundations. *Phys. Rev.* **104**, 1760–1770 (1956), DOI: [10.1103/PhysRev.104.1760](https://doi.org/10.1103/PhysRev.104.1760).
- [47] Hawthorn, D.G., Shen, K.M., Geck, J., Peets, D.C., Wadati, H., Okamoto, J., Huang, S.W., Huang, D.J., Lin, H.J., Denlinger, J.D., Liang, R., Bonn, D.A., Hardy, W.N., & Sawatzky, G.A., Resonant elastic soft x-ray scattering in oxygen-ordered $\text{YBa}_2\text{Cu}_3\text{O}_{6+\delta}$. *Phys. Rev. B* **84**, 075125 (2011), DOI: [10.1103/PhysRevB.84.075125](https://doi.org/10.1103/PhysRevB.84.075125).
- [48] A Mathematica notebook to calculate f1 from tabulated f2 atomic scattering form factors, URL: https://github.com/AJAthesis/KramersKronig_AtomicNIST/.
- [49] Stavitski, E. & de Groot, F.M., The CTM4XAS program for EELS and XAS spectral shape analysis of transition metal L edges. *Micron* **41**, 687–694 (2010), DOI: [10.1016/j.micron.2010.06.005](https://doi.org/10.1016/j.micron.2010.06.005).
- [50] Hawthorn, D.G., He, F., Venema, L., Davis, H., Achkar, A.J., Zhang, J., Sutarto, R., Wadati, H., Radi, A., Wilson, T., Wright, G., Shen, K.M., Geck, J., Zhang, H., Novák, V., & Sawatzky, G.A., An in-vacuum diffractometer for resonant elastic soft x-ray scattering. *Rev. Sci. Instrum.* **82**, 073104 (2011), DOI: [10.1063/1.3607438](https://doi.org/10.1063/1.3607438).
- [51] Design of REIXS beamline, URL: <http://exshare.lightsource.ca/REIXS/Pages/BLDesign.aspx>.
- [52] Basic Demonstration of OrientExpress for orienting a single crystal from a single Laue Photograph, URL: <http://www CCP14.ac.uk/tutorial/lmpg/orientexpress.htm>.